Article

Property Characterization and Photocatalytic Activity Evaluation of BiGdO$_3$ Nanoparticles under Visible Light Irradiation

Jingfei Luan *, Yue Shen, Lingyan Zhang and Ningbin Guo

State Key Laboratory of Pollution Control and Resource Reuse, School of the Environment, Nanjing University, Nanjing 210093, China; yueshen_sally@outlook.com (Y.S.); lingyanzhang2016@sina.com (L.Z.); ningbinguo@sina.com (N.G.)

* Correspondence: jfluan@nju.edu.cn; Tel.: +86-135-8520-6718; Fax: +86-25-8968-0397

Abstract: BiGdO$_3$ nanoparticles were prepared by a solid-state reaction method and applied in photocatalytic degradation of dyes in this study. BiGdO$_3$ was characterized by X-ray powder diffraction, X-ray photoelectron spectroscopy, scanning electron microscopy, Brunauer-Emmett-Teller, UV-Vis diffuse reflectance spectroscopy and transmission electron microscopy. The results showed that BiGdO$_3$ crystallized well with the fluorite-type structure, a face-centered cubic crystal system and a space group *Fm3m 225*. The lattice parameter of BiGdO$_3$ was 5.465 angstrom. The band gap of BiGdO$_3$ was estimated to be 2.25 eV. BiGdO$_3$ showed a strong optical absorption during the visible light region. Moreover, the photocatalytic activity of BiGdO$_3$ was evaluated by photocatalytic degradation of direct dyes in aqueous solution under visible light irradiation. BiGdO$_3$ demonstrated excellent photocatalytic activity in degrading Direct Orange 26 (DO-26) or Direct Red 23 (DR-23) under visible light irradiation. The photocatalytic degradation of DO-26 or DR-23 followed the first-order reaction kinetics, and the first-order rate constant was 0.0046 or 0.0023 min^{-1} with BiGdO$_3$ as catalyst. The degradation intermediates of DO-26 were observed and the possible photocatalytic degradation pathway of DO-26 under visible light irradiation was provided. The effect of various operational parameters on the photocatalytic activity and the stability of BiGdO$_3$ particles were also discussed in detail. BiGdO$_3$/(visible light) photocatalysis system was confirmed to be suitable for textile industry wastewater treatment.

Keywords: BiGdO$_3$; solid state reaction; properties characterization; direct dyes; visible light irradiation; photocatalytic degradation

1. Introduction

Photocatalytic degradation has emerged as an efficient method for purification and treatment of polluted water and air in recent years [1–12]. Compared with conventional methods including physical, chemical and biological processes, photocatalysis was considered to be the most efficient and have a market prospect for the degradation of persistent organic pollutants [13–15]. Therefore, research on all kinds of photocatalysts for efficient photocatalysis has become a hot subject. Titanium dioxide (TiO$_2$) was widely accepted as one of the most promising photocatalysts owing to its high activity, low cost, non toxicity and chemical stability [16–19]. However, TiO$_2$ could only absorb UV light and it was not responding to the visible light area, thus the efficiency of TiO$_2$ was low for utilization of sunlight (4%) [20–22]. UV light occupies only 5% in the solar spectrum, while the visible light between 400 and 750 nm occupies 41%. If the UV light part and the visible light part of sunlight could be fully utilized at the same time, the light quantum efficiency would be greatly improved.

One major direction for preparing efficient visible light photocatalysts is the use of non-metallic elements such as N, S, C, etc. to replace the oxygen element of TiO_2. Element doping could reduce the band gap of the materials to extend its responding area to the visible region of the spectrum, and improved the light quantum efficiency to some extent [23–31]. Another direction is the preparation of composite oxides and complex compounds, such as $rGO/C-MoO_3$, $Co_xZn_{1-x}Fe_2O_4$-rGO, Fe_3O_4@C/Cu, Fe_3O_4@CuO, WO_3/ZnO, $Pt/Au/WO_3$, $Ti/ZnO-Cr_2O_3$, $ZnO/CdS/TiO_2$, $CoO-TiO_2$, $CuO/SnO_2/TiO_2$, $BiPO_4/TiO_2/g-C_3N_4$, $AgInS_2$, $ZnS-AgInS_2$, $Ag_2Mo_4O_{13}$, $K_6Nb_{10.8}O_{30}$, $Y_2Sn_2O_7$, $Ca_2Nb_2O_7$, Bi_2GaTaO_7, ZnO-T, and ZnO nano- and microneedles [32–50] which showed photocatalytic activity under visible light irradiation. These metal oxides as photocatalysts have relatively high photocatalytic activity because of their unique arrangement of electronic structure, charge transport characteristics and light absorption properties, which could generate photoexcited charge carriers and show remarkable stability under varying conditions [51]. Bismuth oxide (Bi_2O_3) is an important p-type semiconductor and has been extensively investigated for various applications owing to its unique optical and electrical properties [52–57]. The band gap of Bi_2O_3 (2.58 eV) is narrower than the band gap of TiO_2 (3.2 eV), thus Bi_2O_3 has been investigated as a visible-light-driven photocatalyst. However, the rapid recombination of the photogenerated electron-hole pairs led to a low activity of Bi_2O_3 [58–60]. Moreover, many bismuth-based mixed oxides such as $BiVO_4$, Bi_2WO_6, $Bi_2Ti_2O_7$, $Bi_{12}TiO_{20}$, and In_2BiTaO_7 [61–69] have been reported to be excellent visible light photocatalysts. The Bi $6s^2$ lone pairs of electron might play an important role in these compounds [70,71].

Some previous reports have shown that Gd^{3+}, a rare earth ion, S doped on the photocatalysts could greatly enhance the photocatalytic activity under visible light irradiation. Guo et al. [72] evaluated the photocatalytic activity of $Bi_{1-x}Gd_xFeO_3$ (x = 0, 0.05, 0.1, and 0.15) for the photodegradation of rhodamine B and the acquired results showed that the low concentration of Gd doping below x = 0.1 could significantly increase the photocatalytic activity of the photocatalysts compared with the pure $BiFeO_3$ nanopowders. Luo et al. [73] reported that Gd-doped porous Bi_2O_3 microspheres, accompanied with different Gd concentrations, 0%, 1%, 2%, 3% and 4%, prepared by a simple hydrothermal synthesis method, could degrade 95.7%, 98.2%, 97.1% and 91.1%, respectively of rhodamine B under visible light irradiation for 120 min, and also could degrade 97.0%, 99.3%, 98.1% and 80.5%, respectively, of methyl orange under visible light irradiation for 28 min, which showed higher photocatalytic activity than the pure β-Bi_2O_3 catalyst. The main effect of rare earth ion Gd^{3+} doping on the photocatalytic activity of the photocatalysts was that Gd^{3+} could trap photoelectrons as efficient scavengers, which decreased the recombination probability of the electron-hole pairs [73–75].

Previous works indicated that photoexcitation of an electron in an O_{2p} and Bi_{6s} hybrid orbital could lead to a charge transfer occurring to a d orbital of the other metal in the composite oxide [76,77]. Gd had one occupied 4d orbital in the ground state and Gd–Bi composite oxide might be responding to the visible light irradiation. In the present paper, $BiGdO_3$ nanoparticles were synthesized by a solid-state reaction method and tested to be efficient for photocatalytic degradation of dyes. The structural, optical and photocatalytic properties of $BiGdO_3$ were studied in detail. This work concentrated on the photocatalytic properties of $BiGdO_3$ for photodegradation of direct dyes in aqueous solution under visible light irradiation. The effect of various operational parameters on the photocatalytic degradation efficiency was examined in detail. The stability of both material and performance of $BiGdO_3$ as a visible light photocatalyst was also investigated by material characterization and the repeated photocatalytic degradation tests. Finally, the degradation intermediates of DO-26 were observed and the possible photocatalytic degradation pathway of DO-26 was studied.

2. Results and Discussion

2.1. Structural and Optical Properties

2.1.1. XRD Analysis

Figure 1 shows the powder X-ray diffraction pattern of $BiGdO_3$ together with full-profile structure refinements of the collected data as obtained by the RIETAN™ [78] program, which was based on the Rietveld analysis. It can be seen in Figure 1 that all the diffraction peaks of the sample were sharp shape and were identical to the standard card (JSPDS 27-1043). It meant that the as-prepared bismuth gadolinium oxide $BiGdO_3$ was single phase and was of high purity. According to the high purity of the precursors that were used in this study, it was unlikely that the observed space groups originate from the presence of impurities. Figure 2 shows the XRD patterns of $BiGdO_3$ prepared at different temperatures. It was clear that $BiGdO_3$ was not formed completely when $BiGdO_3$ was treated at 750 °C for 10 h (as shown in Figure 2a) because there were small peaks which indicated that other phases existed. The reason was that the melting point 820 °C of Bi_2O_3 or the melting point 2330 °C of Gd_2O_3 was higher than 750 °C, as a result, the solid particle of Bi_2O_3 and the solid particle of Gd_2O_3 were difficult to form single phase $BiGdO_3$ by mutual diffusion of the solid phase particles when they were put in the electric furnace with the highest sintering temperature of 750 °C. The characteristic diffraction peaks of the sample which was treated at 1050 °C for 12 h (as shown in Figure 2b) were not so clear compared with the sample which was treated at 750 °C for 10 h, 850 °C for 10 h, and then at 1050 °C for 12 h (as shown in Figure 2c) with an intermediate regrinding process. It showed that, with the three-step treatment procedure, the sintering reaction proceeded completely and a better crystallized $BiGdO_3$ could be obtained. The main reasons were that the solid particle of Bi_2O_3 and the solid particle of Gd_2O_3 did not form single phase at the temperature of 750 °C, and then the grinding process increased the opportunity of high temperature diffusion between Bi_2O_3 and Gd_2O_3. Secondly, Bi_2O_3 melted and Gd_2O_3 did not melt at the temperature of 850 °C. In addition, high temperature diffusion between the molten liquid particle of Bi_2O_3 and the solid particle of Gd_2O_3 was easier to form single phase $BiGdO_3$. Finally, the molten liquid particle of Bi_2O_3 and the solid particle of Gd_2O_3, which remained at the high temperature (1050 °C) for a long time could diffuse evenly and form a purer single phase $BiGdO_3$. Moreover, rapid heating process avoided the formation of the single phase $BiGdO_3$ in the heating intermediate process and guaranteed the single phase $BiGdO_3$ to form beginning at 1050 °C. Furthermore, slow cooling process avoided the particles to become brittle because rapid cooling would result in imperfect crystallization of the single phase $BiGdO_3$ or crystal defect of $BiGdO_3$. In conclusion, the novelty of this method was that the synthesis of the purely single phase $BiGdO_3$ utilized three-step sintering grinding method for the first time.
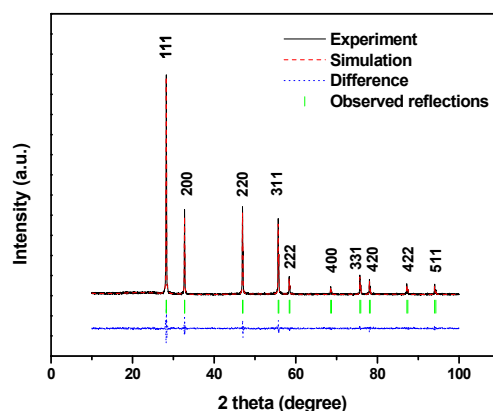

Figure 1. X-ray powder diffraction patterns and Rietveld refinements of $BiGdO_3$. A difference (observed-calculated) profile is shown beneath. The tic marks represent reflection positions.
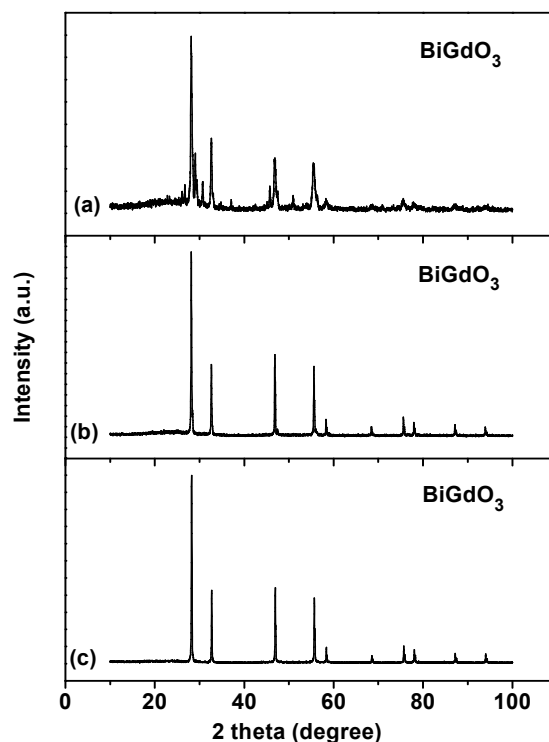
Figure 2. X-ray powder diffraction patterns of $BiGdO_3$ samples prepared at different temperatures: (**a**) sample prepared at 750 °C for 10 h; (**b**) sample prepared at 1050 °C for 12 h; and (**c**) sample prepared at 750 °C for 10 h, 850 °C for 10 h and then at 1050 °C for 12 h with an intermediate regrinding process.

The crystal structure of $BiGdO_3$ was successfully refined by using the Rietveld method from the X-ray diffraction data. The result of the final refinement for $BiGdO_3$ displayed a good agreement between the observed intensities and calculated intensities. As a result, $BiGdO_3$ possessed the fluorite-type structure, a face-centered cubic crystal system and a space group *Fm3m 225* (O atoms were included in the model). The lattice parameter α for $BiGdO_3$ from the refined result was 5.465 angstrom. According to the Bragg Equation (1) and the calculation formula for cubic crystal face spacing Equation (2):

$$2d\sin\theta = \lambda = 1.54056 \tag{1}$$

$$d = a / \left(h^2 + k^2 + l^2 \right)^{1/2} \tag{2}$$

where d was the face spacing, θ was the diffraction angle, and h, k and l were the crystal indices. According to above equations, the lattice parameter α for $BiGdO_3$ was calculated to be 5.472 angstrom, which was close to the refined result. All the diffraction peaks for $BiGdO_3$ could be successfully indexed according to the lattice constant and above space group. The atomic coordinates and structural parameters of $BiGdO_3$ are listed in Table 1. The outcome of the refinement for $BiGdO_3$ generated the R-factor of the Rietveld refinement. R_P factor (unweighted residual error), one of the reliability index parameters, showed the difference between the observed and simulated powder diffraction patterns [79,80]. In our experiments, R_P was 14.14% with space group *Fm3m 225* for $BiGdO_3$. This means that there was small difference between the observed and simulated powder diffraction patterns.

Table 1. Structural parameters of BiGdO$_3$.

Atom	X	Y	Z	Occupation Factor
Bi	0.50000	0.50000	0.50000	1.0
Gd	0.00000	0.00000	0.00000	1.0
O	0.25000	0.00000	0.00000	0.5

2.1.2. XPS Spectra

Figure 3 presents the XPS spectrum of BiGdO$_3$. It was obvious that the observed XPS spectra of BiGdO$_3$ showed neither shoulders nor widening peaks, suggesting (albeit not proving) the absence of any other phases. The sample showed the presence of bismuth (Bi 4f, Bi 4d, and Bi 5d), gadolinium (Gd 3d, Gd 4d, and Gd 4f), oxygen (O 1s) and carbon (C 1s). Moreover, the peak of C 1s was attributed to the surface adsorption pollution. Figure 4 shows the XPS peaks of: Bi 4f (A); Gd 3d (B); O 1s (C); and the split of O 1s (D) in BiGdO$_3$. Various elemental peaks, which correspond to specific binding energies of BiGdO$_3$, are provided in Table 2. The binding energies of Bi 4f$^{5/2}$, Bi 4f$^{7/2}$, Gd 3d$^{3/2}$ and Gd 3d$^{5/2}$ in BiGdO$_3$ were 163.1, 157.8, 1218.2 and 1185.9 eV, respectively. It can be seen in Table 2 that there were two peaks with different binding energies for oxygen (O 1s). The split of O 1s peaks in Figure 4D was assigned to O 1s peaks of crystal lattice oxygen (528.8 eV) and surface adsorbed oxygen (530.4 eV) [81]. Surface adsorbed oxygen might correspond to the hydroxyl oxygen, which was significant for the improvement of the photocatalytic efficiency. Hydroxyl oxygen, which was adsorbed onto the surface of the photocatalyst, was in favor of the generation of hydroxyl radicals.
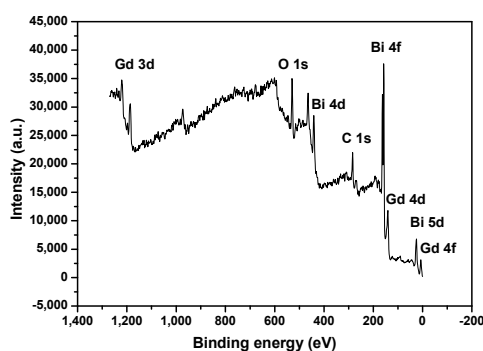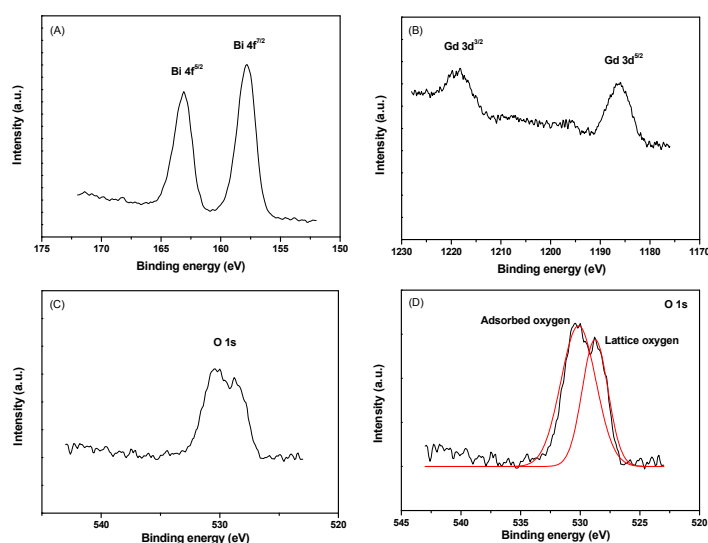

Figure 3. XPS spectrum of BiGdO$_3$.

Figure 4. XPS peaks of: Bi 4f (**A**); Gd 3d (**B**); O 1s (**C**); and split of O 1s (**D**) in BiGdO$_3$.

Table 2. Binding energies of Bi 4f, Gd 3d and O 1s in BiGdO$_3$.

Elements	Bi 4f$^{5/2}$	Bi 4f$^{7/2}$	Gd 3d$^{3/2}$	Gd 3d$^{5/2}$	O 1s
Binding energy (eV)	163.1	157.8	1218.2	1185.9	528.8

For BiGdO$_3$, surface elemental analysis revealed that the average atomic ratio of Bi:Gd:O is 10.33:9.87:42.84. The ratio of Bi:Gd in the sample was almost the ratio of 1:1. The value of oxygen was high because there was a lot of adsorbed oxygen on the surface.

2.1.3. TEM and SEM Analyses

The morphology and microstructure of the as-prepared sample were examined by TEM, SEM and EDS. Figure 5 displays the TEM and SEM image of BiGdO$_3$. We could observe from the images of BiGdO$_3$ that the particles presented nanoscale and irregular-shaped appearance and that the distribution was relatively uniform. The average particle size of BiGdO$_3$ approached 750 nm.

Figure 6 shows the EDS spectrum of BiGdO$_3$. The EDS spectrum that was taken from the prepared BiGdO$_3$ displayed the presence of bismuth, gadolinium and oxygen. Moreover, the peak of C was attributed to surface adsorption pollution. Other elements could not be identified from BiGdO$_3$. The ratio of Bi:Gd:O in BiGdO$_3$ sample was 12.57:12.88:39.53, which was accordant with the ratio of 1:1:3 expected from the BiGdO$_3$ molecular formula. The results further indicated that the oxidation state of Bi, Gd and O ions from BiGdO$_3$ were +3, +3 and -2, respectively. According to the above available data, it could be concluded that the sample which was prepared with Bi$_2$O$_3$ and Gd$_2$O$_3$ in a solid state reaction was BiGdO$_3$, which was in agreement with the results of XRD and XPS analyses.
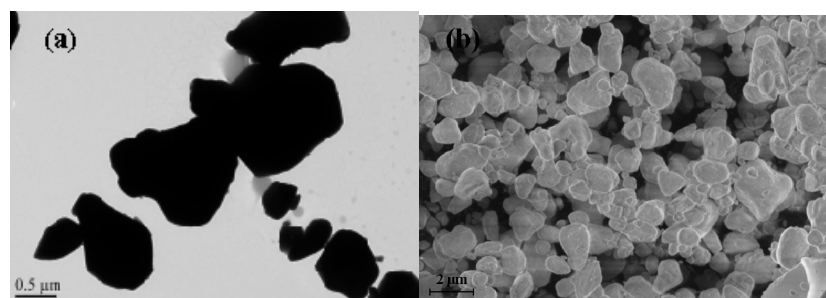
Figure 5. (**a**) TEM image of BiGdO$_3$; and (**b**) SEM image of BiGdO$_3$.
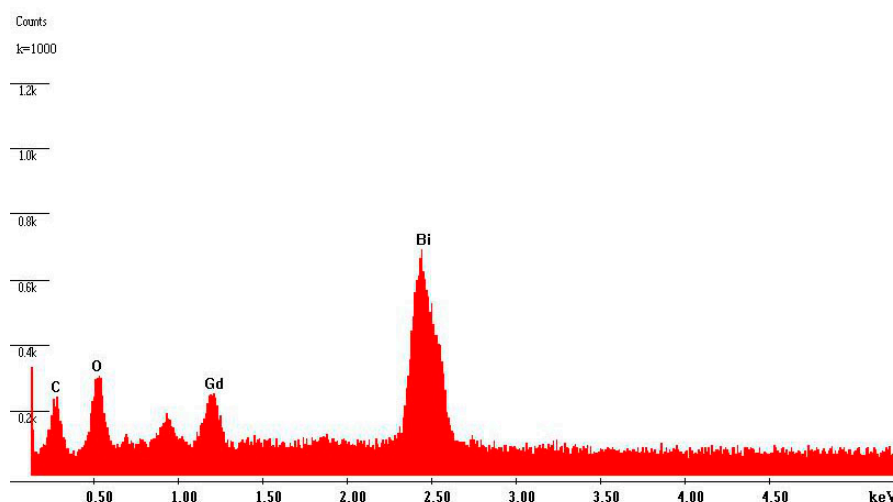
Figure 6. EDS spectrum of BiGdO$_3$.

2.1.4. BET Analysis

The specific surface area detected by the BET isotherm measurements was 3.25 m$^2 \cdot$g^{-1} for BiGdO$_3$. The specific surface area of BiGdO$_3$ was almost 14 times smaller than that of TiO$_2$, which was measured to be 46.24 m$^2 \cdot$g^{-1}. Many catalysts that are produced by solid state methods often exhibit low surface area, but might own good photocatalytic activity. Photocatalytic materials LiBi$_4$M$_3$O$_{14}$ (M = Nb, Ta) that were prepared by Muktha et al. [82] showed reasonable photocatalytic activity for degrading dyes and organic compounds, despite their low BET surface area (0.3 or 0.1 m$^2 \cdot$g^{-1}).

2.1.5. UV-Vis Diffuse Reflectance Spectra

UV-Vis diffuse reflectance spectroscopy was carried out to investigate the optical properties of the photocatalyst sample. Figure 7a presents the UV-Vis diffuse reflectance spectrum of BiGdO$_3$, Bi$_2$O$_3$, Gd$_2$O$_3$ and TiO$_2$. For a comparison, the UV-Vis diffuse reflectance spectra of Bi$_2$O$_3$, Gd$_2$O$_3$ and TiO$_2$ were also provided in Figure 7a. As we all know, the well-known TiO$_2$ whose absorption edge was at less than 380 nm had no response to the visible light irradiation. It could be seen that the absorption edge of BiGdO$_3$ was found to be at 585 nm, which belonged to the visible region of the spectrum. It was obvious that the as-prepared BiGdO$_3$ exhibited absorption range extending from the UV light region to 600 nm, which was wider than the range of Bi$_2$O$_3$. We could draw a conclusion from the researches reported by Oshikiri et al. [83] and Zheng et al. [84] that the positions and width of the conduction band and the valence band of BiGdO$_3$ could be investigated by calculating the electronic band structure of Bi$_2$O$_3$, Gd$_2$O$_3$ and BiGdO$_3$ with the plane-wave-based density functional method. Moreover, the band structure calculations of Bi$_2$O$_3$, Gd$_2$O$_3$ and BiGdO$_3$ might be performed with the program of Cambridge serial total energy package (CASTEP) and first-principles simulation [85]. The CASTEP calculation was composed of the plane-wave pseudopotential total energy method according to the density functional theory. The valence band of Bi$_2$O$_3$ or Gd$_2$O$_3$ was composed of 2p orbital of oxygen, while the conduction band of Bi$_2$O$_3$ or Gd$_2$O$_3$ was composed of 6p orbital of bismuth or 5d orbital and 6s orbital of gadolinium, respectively. Our previous works similarly explained [85,86] that the conduction band of the BiGdO$_3$ photocatalyst consisted mainly of Gd 5d orbital component, while the valence band of BiGdO$_3$ consisted of mainly O 2p orbital component, Bi 6p orbital component and Gd 6s orbital component. The contribution of the valence band on the value of band gap of the BiGdO$_3$ photocatalyst was mainly owing to the hybridization among Bi 6p orbital component, Gd 5d orbital component and Gd 6s orbital component. The top of the value band of BiGdO$_3$ increased and the distance between the top of the valence band of BiGdO$_3$ and the bottom of the conduction band of BiGdO$_3$ decreased. This change caused the decrease of band gap of the BiGdO$_3$ photocatalyst, which was the main reason for the red-shift of the spectrum for BiGdO$_3$. Another possible reason was the different electronic structures of Bi$_2$O$_3$, Gd$_2$O$_3$ and BiGdO$_3$.
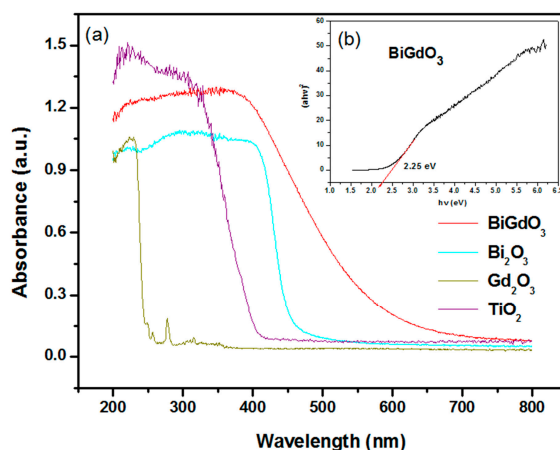

Figure 7. (**a**) UV-Vis diffuse reflectance spectra of BiGdO$_3$, Bi$_2$O$_3$, Gd$_2$O$_3$ and TiO$_2$; and (**b**) plot of $(\alpha h\nu)^{1/n}$ versus $h\nu$ for BiGdO$_3$ (inset).

For a crystalline semiconductor, the optical absorption near the band edge followed the equation [87,88]:

$$\alpha h\nu = A \left(h\nu - E_g \right)^n \tag{3}$$

where A, α, E_g and ν were proportional constant, absorption coefficient, band gap and light frequency respectively. Within this equation, n determined the character of the transition in a semiconductor. E_g and n could be calculated by the following steps: (i) plotting $\ln(\alpha h\nu)$ versus $\ln(h\nu-E_g)$ by assuming an approximate value of E_g; (ii) deducing the value of n based on the slope in this graph; and (iii) refining the value of E_g by plotting $(\alpha h\nu)^{1/n}$ versus $h\nu$ and extrapolating the plot to $(\alpha h\nu)^{1/n} = 0$. According to this method, the inset in Figure 7b shows the plot of $(\alpha h\nu)^{1/n}$ versus $h\nu$ for BiGdO$_3$. The band gap of BiGdO$_3$ was calculated to be 2.25 eV according to above equation, while the value of n for BiGdO$_3$ was 0.5, indicating that the optical transition for BiGdO$_3$ is directly allowed. Furthermore, the band gap of Bi$_2$O$_3$ was calculated to be 2.65 eV. Thus, the above results indicated an enhanced visible light absorption of BiGdO$_3$ and a narrower band gap compared with Bi$_2$O$_3$.

2.2. Evaluation of Photocatalytic Activity

The photocatalytic activities of the as-prepared BiGdO$_3$ samples were evaluated by the degradation of Direct Orange 26, Direct Red 23 or phenol under visible light irradiation. Direct Orange 26, Direct Red 23 or phenol was degraded well by using BiGdO$_3$ as a photocatalyst under visible light irradiation. The effect of various operational parameters, namely, catalyst loading, initial concentration of Direct Orange 26 or Direct Red 23, pH value, light intensity and coexisting ions on the photocatalytic degradation efficiency was investigated in detail.

2.2.1. Photocatalytic Degradation of Direct Orange 26 or Direct Red 23 or Phenol

Figure 8 shows the comparison of removal efficiencies between Direct Orange 26 and Direct Red 23 under different conditions. As shown in Figure 8, the suspension had already reached adsorption/desorption equilibrium between the dye and the catalyst when stirred in the dark for 30 min, maintaining the decolorization rate of 31% for Direct Orange 26 (obtained from Figure 8A) and the decolorization rate of 23% for Direct Red 23 (obtained from Figure 8B) using BiGdO$_3$ as a photocatalyst when stirred in the dark for 360 min. It could be concluded from the observation of the color of the catalyst that the adsorption process was just physical adsorption. The BiGdO$_3$ particles changed to deep orange or red after the adsorption process while the particles still presented their original color after photocatalytic reaction, which meant that the adsorbed dye was also degraded during the reaction. It can be seen in Figure 8 that the photocatalytic degradation efficiency was 83.7% for Direct Orange 26 and 60.8% for Direct Red 23 using BiGdO$_3$ as a photocatalyst under visible light irradiation within 360 min, while the photocatalytic degradation efficiency was 39.8% for Direct Orange 26 and 37.1% for Direct Red 23 using Bi$_2$O$_3$ as a catalyst or 16.3% for Direct Orange 26 and 21.8% for Direct Red 23 using Gd$_2$O$_3$ as a catalyst under visible light irradiation within 360 min. It can be seen in Figure 7a that Gd$_2$O$_3$ had no visible light response, but Gd$_2$O$_3$ did have a faint degradation efficiency on Direct Orange 26 or Direct Red 23 under visible light irradiation. The possible reasons of this phenomenon were the adsorption of the Gd$_2$O$_3$ sample and the photosensitive effect of Direct Orange 26 or Direct Red 23. These catalysts could be arranged in order of increasing degradation efficiency during the same reaction time: Gd$_2$O$_3$ < Bi$_2$O$_3$ < BiGdO$_3$. The results in Figure 8 indicate that BiGdO$_3$ had better photocatalytic activities for Direct Orange 26 or Direct Red 23 than Bi$_2$O$_3$ or Gd$_2$O$_3$. The cost of 100 g Gd$_2$O$_3$ and Bi$_2$O$_3$ was 63.2 dollars and 64.5 dollars, respectively, while the synthesis of 100 g pure BiGdO$_3$ catalyst totally cost about 71 dollars, indicating that BiGdO$_3$ had higher cost performance than Bi$_2$O$_3$ and Gd$_2$O$_3$. Additionally, there was almost no decrease for the UV-Vis absorbance signal of Direct Orange 26 or Direct Red 23 that was obtained under visible light irradiation in the absence of a photocatalyst.

In order to quantitatively understand the reaction kinetics of the degradation of Direct Orange 26 or Direct Red 23, a pseudo first order was utilized to fit the experimentally obtained data. Figure 9 presents the reaction kinetics of the photocatalytic degradation of Direct Orange 26 or Direct Red 23 by using $BiGdO_3$ as a photocatalyst. The pseudo first order indicated a linear correlation between $\ln(C_o/C)$ and the visible light irradiation time. In the above equation, C represents the dye concentration at time t, and C_o represents the initial dye concentration. On the basis of the correlation result between $\ln(C_o/C)$ and the irradiation time, the first-order rate constant k was estimated to be 0.0046 min^{-1} for Direct Orange 26. For Direct Red 23, the first-order rate constant k was estimated to be 0.0023 min^{-1}, which was smaller than that for Direct Orange 26.

Figure 10 shows the degradation rate of phenol by using $BiGdO_3$ as catalyst under visible light irradiation with respect to time. It can be seen in Figure 10 that the photocatalytic degradation rate of phenol was very low and could be ignored without adding $BiGdO_3$ as a photocatalyst. Obviously, we could observe that an improved activity was also obtained when colorless phenol was also selected as a contaminant model with $BiGdO_3$ as catalyst. The photocatalytic degradation efficiency of phenol was 59.8% by using $BiGdO_3$ as a photocatalyst under visible light irradiation after 360 min, indicating that the catalyst $BiGdO_3$ itself had photocatalytic activity and that the photodegradation process of Direct Orange 26 or Direct Red 23 by using $BiGdO_3$ as a photocatalyst was not mainly due to photosensitive effect [89]. The above results revealed that the as-prepared catalyst $BiGdO_3$ could decompose dye Direct Orange 26 or Direct Red 23 efficiently, at the same time, $BiGdO_3$ could also degrade non-dye compounds, such as phenol. Ao et al. [90] used the same verification method to prove that the photodegradation process of dye by using as-prepared photocatalyst was not mainly due to the photosensitive effect.
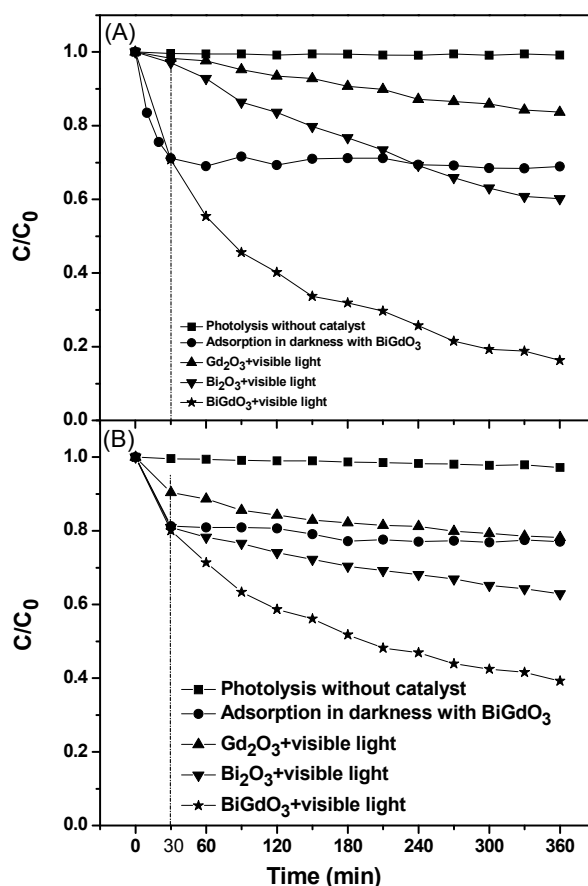

Figure 8. Comparison of removal efficiencies between Direct Orange 26 (**A**) and Direct Red 23 (**B**) under different conditions.
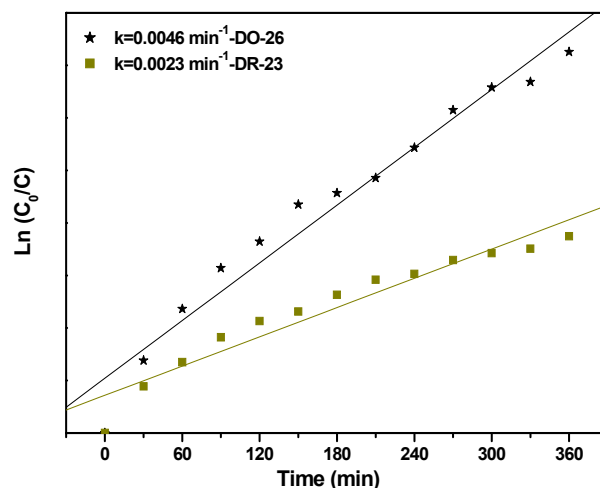
Figure 9. The first-order kinetic plots for the photocatalytic degradation of Direct Orange 26 or Direct Red 23 using $BiGdO_3$ as a photocatalyst.
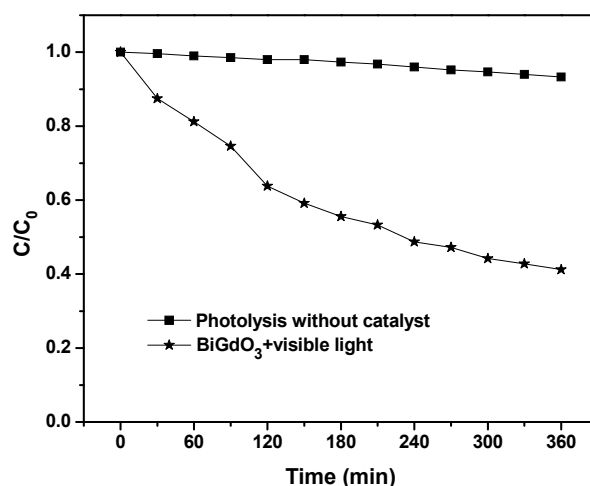

Figure 10. Photocatalytic activity of $BiGdO_3$ for degrading phenol under visible light irradiation.

2.2.2. Effect of Various Operational Parameters

Figure 11 presents the effect of the catalyst loading on the photocatalytic degradation efficiency of Direct Orange 26 or Direct Red 23. The catalyst loading varied from 0.4 to 1.6 g/L with the initial concentration of 30 mg/L from Direct Orange 26 or Direct Red 23 and the original pH value of 6.2 from Direct Orange 26 or Direct Red 23. It can be seen in Figure 11 that the photocatalytic degradation efficiency of Direct Red 23 slightly increased while the catalyst loading increased from 0.4 to 1.6 g/L. The photocatalytic degradation efficiency of Direct Orange 26 increased while the catalyst loading increased from 0.4 to 1.2 g/L but decreased when the catalyst loading increased further to 1.6 g/L. The decrease of degradation efficiency for above dyes with increasing catalyst loading could be attributed to the increased opacity of the solution, which hindered the light transmission through the solution. Owing to the decrease of the effective light intensity, the photo generation of electrons and positive holes would be reduced and then the photocatalytic degradation efficiency of above dyes was also reduced [91,92]. With the catalyst loading of 1.2 g/L, the photocatalytic degradation efficiency of Direct Orange 26 was 87.1% which was a little higher than 83.7% with the catalyst loading of 1.0 g/L. Therefore, taking both the economic and efficient factors into consideration, the catalyst loading of 1.0 g/L was chosen as optimum loading content.
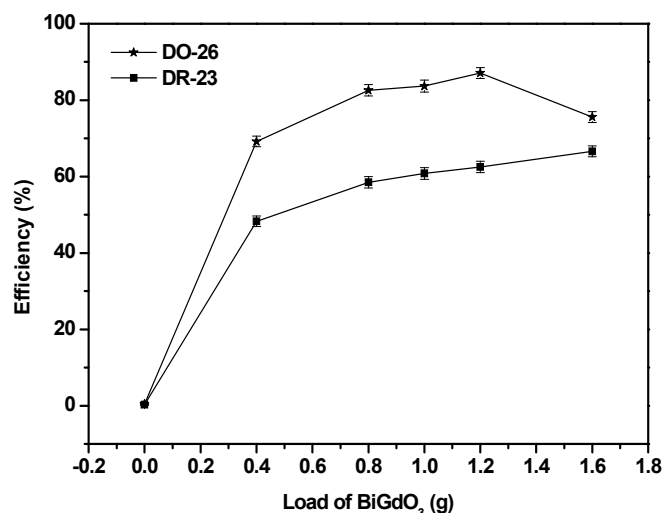
Figure 11. Effect of the catalyst loading on the photocatalytic degradation efficiency of Direct Orange 26 or Direct Red 23.

Figure 12 describes the effect of the initial concentration of Direct Orange 26 or Direct Red 23 on the photocatalytic degradation of Direct Orange 26 or Direct Red 23. With the initial catalyst loading of 1.0 g/L and the original pH value of 6.2 within the dye solution, the initial concentration of Direct Orange 26 or Direct Red 23 varied from 10 to 100 mg/L. It was found from Figure 12 that with increasing the initial concentration of Direct Orange 26 or Direct Red 23, the degradation efficiency of Direct Orange 26 or Direct Red 23 decreased. The main reason was that with increasing the concentration of above dyes, the amount of organic species which would be degraded increased [93], but the photocatalyst loading, the generation amount of e^-/h^+ pairs, dissolved oxygen concentration, intensity of light illumination and light illumination time were constant during the photocatalytic degradation process. Another reason was that the high concentration of Direct Orange 26 or Direct Red 23 reduced the light transmittance possibility towards the solution [94]. Thus, when increasing the initial concentration of Direct Orange 26 or Direct Red 23, the photocatalytic degradation efficiency of above dyes decreased. Comprehensively, considering the total pollutant removal efficiency and suitable reaction time, the initial concentration of 30 mg/L for Direct Orange 26 or Direct Red 23 was selected in the following reactions.
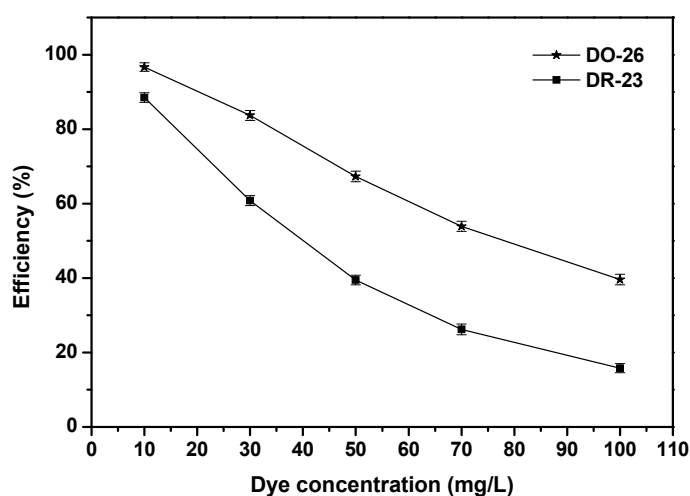

Figure 12. Effect of the initial concentration of Direct Orange 26 or Direct Red 23 on the photocatalytic degradation of Direct Orange 26 or Direct Red 23.

Solution with the initial concentration of 30 mg/L for Direct Orange 26 or Direct Red 23 and catalyst loading of 1.0 g/L was utilized to investigate the effect of the initial pH value on the photocatalytic degradation efficiency of Direct Orange 26 or Direct Red 23. Figure 13 shows the effect of the initial pH value on the photocatalytic degradation efficiency of Direct Orange 26 or Direct Red 23. The initial pH value of Direct Orange 26 solution or Direct Red 23 solution varied from 4 to 12 by utilizing the solution of HCl or NaOH. As shown in Figure 13, the degradation efficiency of Direct Orange 26 or Direct Red 23 increased with decreasing pH value within acidic pH value range and the degradation efficiency of Direct Orange 26 or Direct Red 23 achieved the highest at the pH value of 4. During alkaline pH value range, with the increase of pH value, the degradation efficiency of Direct Orange 26 or Direct Red 23 firstly decreased and then increased. The minimum degradation efficiency of Direct Orange 26 or Direct Red 23 was found to be at the pH value of 10. The effect of the initial pH value was significantly important and generally complex in photocatalytic degradation of organic pollutants [81]. It was reported that the effect of the initial pH value on the photocatalytic degradation efficiency of organic pollutants performed mainly on surface adsorption, the aggregation of the catalyst and the band position of the catalyst in the solution [95,96]. The initial pH value could directly affect the nature of the charge, which was carried by the catalyst surface and the adsorption behavior of the pollutant on the catalyst surface. In addition, direct dyes were easily adsorbed on to the surface of the catalysts under strong acidic condition. Therefore, strong acidic condition was better for excellent photocatalytic degradation of direct dyes according to above results. Moreover, there were a lot of OH^- anions, which existed in the solution when the pH value was from 10 to 12. The h^+ could easily react with a large amount of OH^- for generating active ·OH species which could increase the photocatalytic degradation efficiency of Direct Orange 26 or Direct Red 23 [97–100]. Therefore, the degradation efficiency of Direct Orange 26 or Direct Red 23 could increase during strong alkaline pH value range.

In order to investigate the effect of the visible light intensity on the photocatalytic degradation efficiency of Direct Orange 26 or Direct Red 23, two kinds of light source were applied in the reaction system. Figure 14 shows the effect of the light intensity on the photocatalytic degradation efficiency of Direct Orange 26 and the first-order kinetic plots for the photocatalytic degradation of Direct Orange 26 with different light intensity under visible light irradiation. As shown in Figure 14A, the photocatalytic degradation of Direct Orange 26 with a 500 W Xe arc lamp performed better than that with a 250 W Xe arc lamp. The photocatalytic degradation efficiency of Direct Orange 26 with a 500 W Xe arc lamp was 83.7% while that with a 250 W Xe arc lamp was only 56.9% after visible light irradiation of 360 min. The reaction kinetics of the photocatalytic degradation of Direct Orange 26 with BiGdO$_3$ as a photocatalyst under different light irradiation conditions were clearly demonstrated in Figure 14B. According to the correlative result between $\ln(C_o/C)$ and the light irradiation time, the first-order rate constant k was estimated to be 0.0019 min^{-1} with a 250 W Xe arc lamp as light source. While the first-order rate constant k was estimated to be 0.0046 min^{-1} with a 500 W Xe arc lamp as light source, indicating that the photocatalytic activity of the BiGdO$_3$ sample was significantly improved by using a high-power light source. Figure 15 shows the effect of the light intensity on the photocatalytic degradation efficiency of Direct Red 23 and the first-order kinetic plots for the photocatalytic degradation of Direct Red 23 with different light intensity under visible light irradiation. Similarly, the photocatalytic degradation of Direct Red 23 with a 500 W Xe arc lamp performed better than that with a 250 W Xe arc lamp as shown in Figure 15. The photocatalytic degradation efficiency of Direct Red 23 with a 500 W Xe arc lamp was 60.8% and the first-order rate constant k was estimated to be 0.0023 min^{-1} after visible light irradiation of 360 min. While with a 250 W Xe arc lamp as light source, the photocatalytic degradation efficiency of Direct Red 23 was 48.4% and the first-order rate constant k was estimated to be 0.0016 min^{-1} after visible light irradiation of 360 min. The main reason of this observation which was reported by previous studies was that higher light intensity provided more photons within a given time, accelerated photolytic reaction ratio, and thus made it possible to achieve maximum degradation yield [101–103].
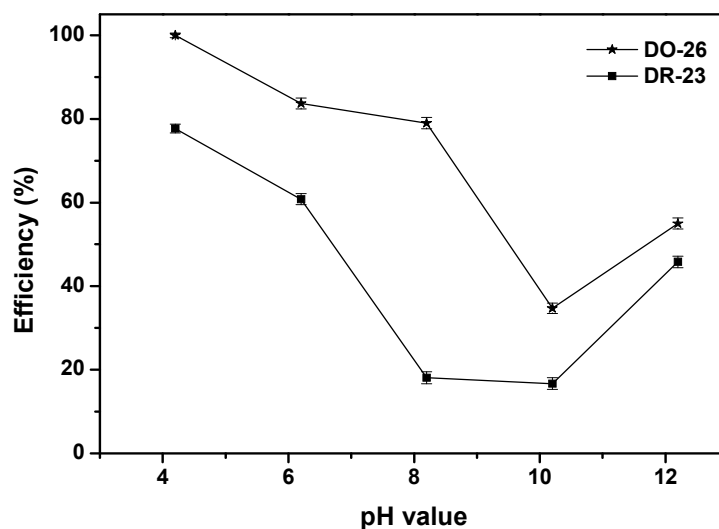
Figure 13. Effect of the initial pH value on the photocatalytic degradation efficiency of Direct Orange 26 or Direct Red 23.
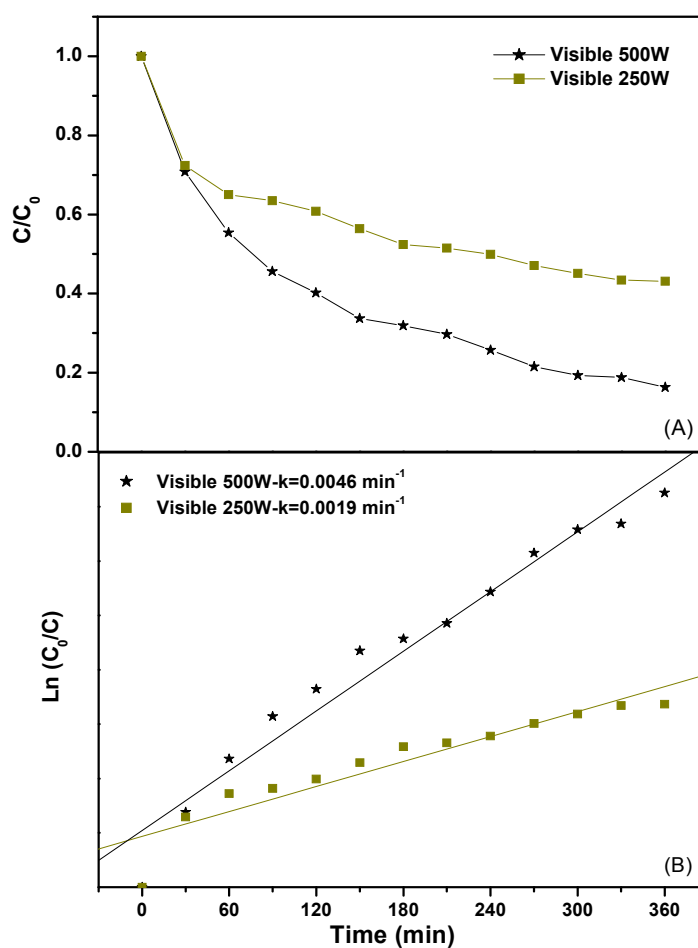

Figure 14. Effect of the light intensity on the photocatalytic degradation efficiency of Direct Orange 26 (**A**); and the first-order kinetic plots for the photocatalytic degradation of Direct Orange 26 (**B**) with different light intensity under visible light irradiation.
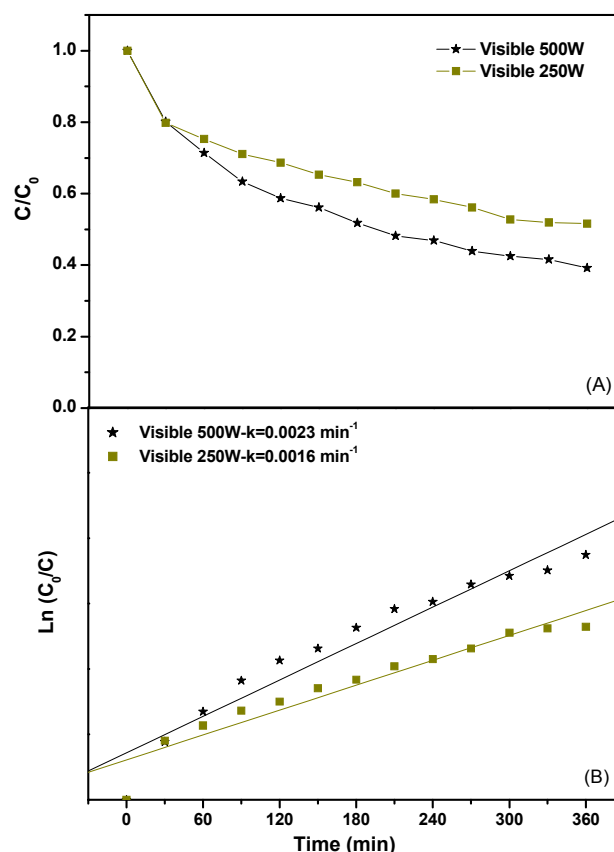
Figure 15. Effect of the light intensity on the photocatalytic degradation efficiency of Direct Red 23 (**A**); and the first-order kinetic plots for the photocatalytic degradation of Direct Red 23 (**B**) with different light intensity under visible light irradiation.
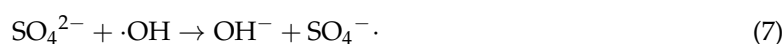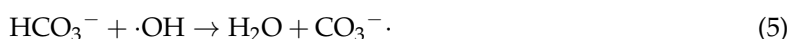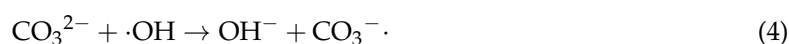
2.2.3. Effect of Coexisting Salts

Composition of actual dye wastewater was very complicated and might contain several salts with different concentrations. In addition, all kinds of salts, which were contained within the dye wastewater, might exert negative or positive influence on the photocatalytic degradation efficiency of dye pollutants. Figure 16 shows the effect of the presence of the coexisting salts on the photocatalytic degradation efficiency of Direct Orange 26. The amount of each salt varied from 0.1 to 2.0 g/L. It can be clearly seen in Figure 16 that the salts had different effect on the photocatalytic degradation efficiency of Direct Orange 26. In case of NaCl, the photocatalytic degradation efficiency of Direct Orange 26 increased with increasing the amount of NaCl and obtained the maximum value with an optimal dosage of 0.5 g/L. On the contrary, both of Na_2SO_4 and Na_2CO_3 had a detrimental effect on the photocatalytic degradation efficiency of Direct Orange 26. With increasing the amount of Na_2SO_4, the degradation efficiency of Direct Orange 26 decreased gently. Similar trend was observed for the photocatalytic degradation of diazo dyes [100,104]. As to Na_2CO_3, the degradation efficiency of Direct Orange 26 decreased suddenly when Na_2CO_3 of 0.1 g/L was added to the solution. The negative effect could be attributed to the reason that CO_3^{2-} and SO_4^{2-} anions inhibited the photocatalytic activity of $BiGdO_3$ by trapping $^\bullet OH$ or h^+ in the reaction system [105–108]. The pH value of the solution varied from 6.2 to 9.1 with the amount of Na_2CO_3 which varied from 0 to 2.0 g/L. It can be seen in Figure 13 that the photocatalytic degradation efficiency of Direct Orange 26 gradually decreased when the pH value varied from 4.2 to 10.2. Moreover, CO_3^{2-} ions addition brought about pH changes that weakened the adsorption of Direct Orange 26 on $BiGdO_3$ and inhibited the photocatalytic oxidation [109]. The following Equations (4)–(7) show the scavenging properties of carbonate ion and sulfate ion.

$$CO_3{}^{2-} + \cdot OH \rightarrow OH^- + CO_3{}^- \cdot \tag{4}$$

$$HCO_3{}^- + \cdot OH \rightarrow H_2O + CO_3{}^- \cdot \tag{5}$$

$$SO_4{}^{2-} + h^+ \rightarrow SO_4{}^- \cdot \tag{6}$$

$$SO_4{}^{2-} + \cdot OH \rightarrow OH^- + SO_4{}^- \cdot \tag{7}$$

Though $SO_4{}^{2-}$ played a negative role during the photocatalytic degradation process of Direct Orange 26, the $SO_4{}^{-\bullet}$ which was produced in Equations (6) and (7) could increase the photocatalytic degradation efficiency of Direct Orange 26 by trapping the photogenerated electrons and/or generating hydroxyl radical (Equations (8) and (9)).

$$SO_4{}^- \cdot + e^- \rightarrow SO_4{}^{2-} \tag{8}$$

$$SO_4{}^- \cdot + H_2O \rightarrow \cdot OH + SO_4{}^{2-} + H^+ \tag{9}$$

According to Equations (6) and (7), we acquired a result that generating a certain amount of $SO_4{}^{-\bullet}$ would consume an equal amount of $^\bullet OH$ or h^+. Although $SO_4{}^{-\bullet}$ was a strong oxidant, the activity and the amount of product $SO_4{}^{-\bullet}$ was less than the activity and the amount of $^\bullet OH$ or h^+ [110]. Thus, $SO_4{}^{-\bullet}$ anions resulted in a mild decrease for the photocatalytic degradation efficiency of Direct Orange 26 compared with $CO_3{}^{2-}$ anions. Cl^- was also reported to have negative influence on the photocatalytic degradation efficiency of dye pollutants because Cl^- was a reducing agent and competed with dye molecules for holes [109,111]. The hole scavenging property for chloride ion was shown in the following Equations (10) and (11).

$$Cl^- + h^+ \rightarrow Cl \cdot \tag{10}$$

$$Cl \cdot + Cl^- \rightarrow Cl_2{}^- \cdot \tag{11}$$

While chlorine radicals formed slowly, they were instantaneously turned to chloride radical anions. However, situation was different that the existing of Cl^- increased the degradation efficiency of Direct Orange 26 in this experimental case. During the dyeing process of direct dyes, sodium chloride and sodium sulfate were usually utilized to improve the dyeing efficiency of the direct dyes. It was supposed that the existing of Cl^- anions or $SO_4{}^{2-}$ anions might promote the aggregation of dyes to the surface of the catalysts. Thus, in the case of NaCl, the increase of the degradation efficiency for Direct Orange 26 might be attributed to the effect of good adsorption.
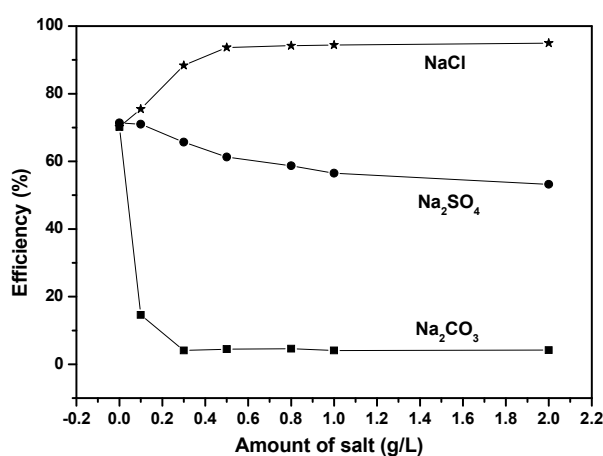

Figure 16. Effect of the coexisting salts on the photocatalytic degradation efficiency of Direct Orange 26.

In order to remove negative effects which originated from the formation of sulfate and carbonate ions in the photocatalytic degradation process, we presented the desulfurization system or adjusted the pH value of the solution. Moreover, we also utilized $BaCl_2$ to remove sulfate and carbonate ions in the photocatalytic system by using $BiGdO_3$ as a photocatalyst under visible light irradiation.

2.2.4. Stability of $BiGdO_3$

In order to study the stability of both material and performance for $BiGdO_3$ as a visible light catalyst, property characterization of $BiGdO_3$ and repeated photocatalytic degradation tests of Direct Orange 26 were carried out. The structure of $BiGdO_3$ after photocatalytic degradation of Direct Orange 26 under different conditions was examined by measuring the XRD patterns of every $BiGdO_3$ sample. Figure 17 presents the X-ray powder diffraction patterns of all $BiGdO_3$ samples that contain the original $BiGdO_3$ sample and the $BiGdO_3$ sample that was obtained after photocatalytic degradation of Direct Orange 26. It can be seen in the XRD patterns (Figure 17) that the XRD pattern of the $BiGdO_3$ sample after the photocatalytic degradation of Direct Orange 26 was the same as that of the original $BiGdO_3$ sample.
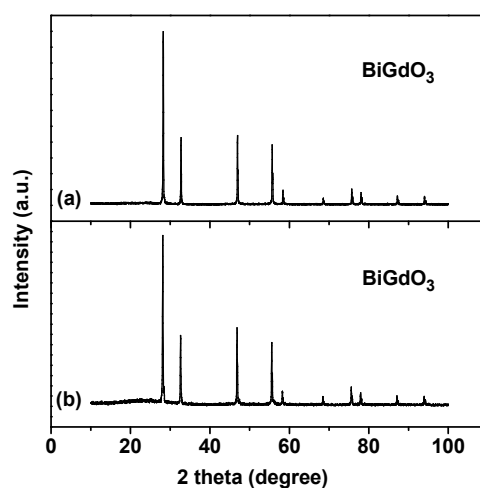

Figure 17. X-ray powder diffraction patterns of every $BiGdO_3$ sample: (**a**) the original $BiGdO_3$ sample; and (**b**) the $BiGdO_3$ sample after photocatalytic degradation of Direct Orange 26.

Figure 18 presents the X-ray powder diffraction patterns of all $BiGdO_3$ samples that are obtained after photocatalytic degradation of Direct Orange 26 by adding salts or adding alkali or adding acid. According to the characteristic diffraction peaks as shown in Figure 18, changes could not be observed compared with the peaks of the original $BiGdO_3$ sample. Namely, the crystal structure of $BiGdO_3$ was stable when acid or alkali or salt was added to the dye solution. The above results clearly indicated the excellent stability of the as-prepared $BiGdO_3$.

Figure 19 presents the repeated photocatalytic degradation tests of Direct Orange 26 with $BiGdO_3$ as photocatalyst under visible light irradiation. The photocatalytic degradation of Direct Orange 26 with $BiGdO_3$ as photocatalyst under visible light irradiation was repeated four times. It can be seen in Figure 19 that the removal efficiencies of Direct Orange 26 were 82.9%, 79.7% and 78.9% for the second, third and fourth cycles respectively, after visible light irradiation of 360 min. It can be seen in Figure 19 that the activity slightly decreased after the first cycle, which was probably due to the drop of a small amount of $BiGdO_3$ particles. Furthermore, the crystal structure of $BiGdO_3$ was stable and the morphology of $BiGdO_3$ did not change after every repeated cycles. Although the photocatalytic degradation efficiency of Direct Orange 26 for the repeated cycles slightly decreased compared with the photocatalytic degradation efficiency of 83.7% for Direct Orange 26 that was obtained from the first-cycle result, $BiGdO_3$ still showed excellent stability and was considered to be an efficient photocatalyst.
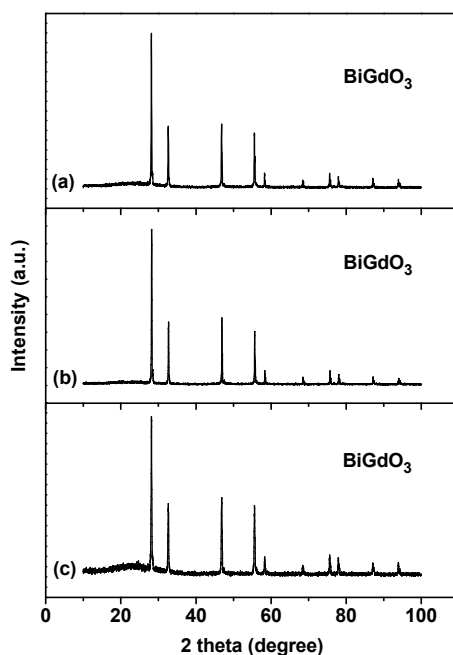
Figure 18. X-ray powder diffraction patterns of all $BiGdO_3$ samples after photocatalytic degradation of Direct Orange 26 under different conditions: (**a**) adding salts; (**b**) adding alkali; and (**c**) adding acid.
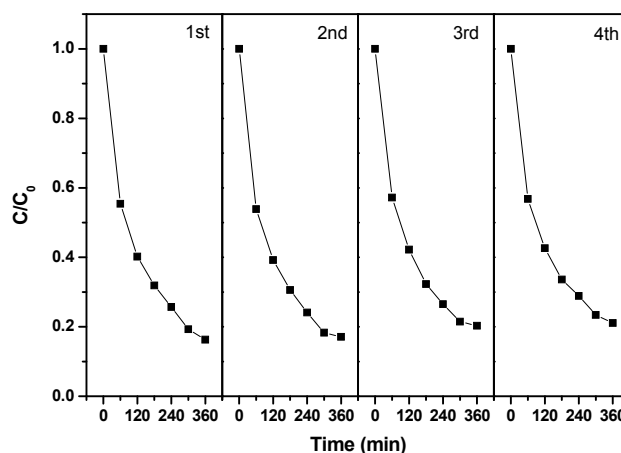

Figure 19. Repeated photocatalytic degradation tests of Direct Orange 26 with $BiGdO_3$ as catalyst under visible light irradiation.

Figure 20 shows the change of TOC concentration during photocatalytic degradation of Direct Orange 26 and Direct Red 23 with $BiGdO_3$ as photocatalyst under visible light irradiation. The TOC measurements revealed the disappearance of organic carbon in the Direct Orange 26 solution or Direct Red 23 solution which contained $BiGdO_3$. The results indicated that 81.49% of TOC decrease was obtained during photocatalytic degradation of Direct Orange 26 after visible light irradiation for 360 min when $BiGdO_3$ was utilized as photocatalyst. In addition, it can also be seen in Figure 20 that 59.19% of TOC decrease was obtained during photocatalytic degradation of Direct Red 23 after visible light irradiation for 360 min with $BiGdO_3$ as catalyst. Therefore, the above results showed that Direct Orange 26 was more easily to be mineralized compared with Direct Red 23 with $BiGdO_3$ as catalyst under visible light irradiation. According to the results in Figures 8 and 20, it could be found that the photodegradation intermediate products of Direct Orange 26 or Direct Red 23 appeared during the photocatalytic degradation of Direct Orange 26 or Direct Red 23 under visible light irradiation.
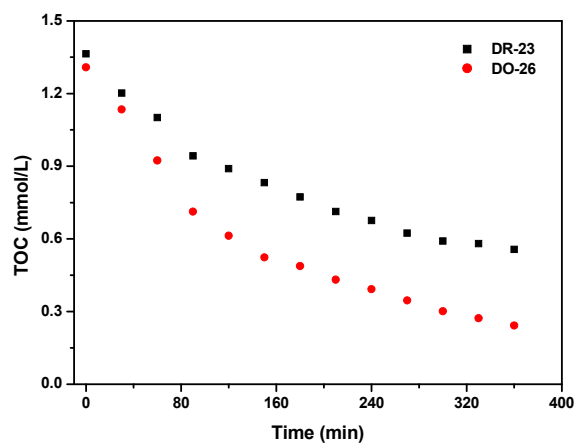
Figure 20. The change of TOC concentration during photocatalytic degradation of Direct Orange 26 and Direct Red 23 with BiGdO$_3$ as catalyst under visible light irradiation.
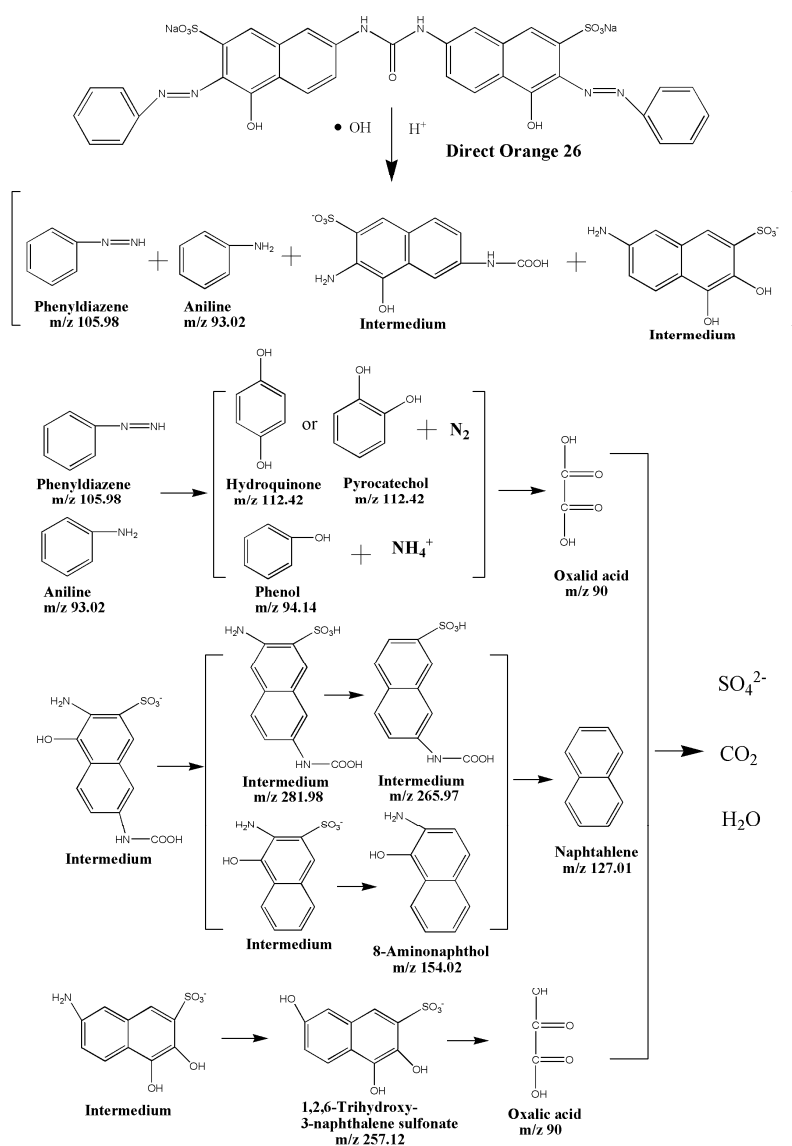

Figure 21. Suggested photocatalytic degradation pathway scheme for Direct Orange 26 under visible light irradiation with BiGdO$_3$ as catalyst.

In our experiments, the identified photodegradation intermediate products of Direct Orange 26 with $BiGdO_3$ as photocatalyst under visible light irradiation were identified as phenyldiazene (m/z: 105.98), phenol (m/z: 94.14), pyrocatechol (m/z: 112.42), 1,2,6-trihydroxy-3-naphthalene sulfonate (m/z: 257.12), oxalic acid (m/z: 90), 8-aminonaphthol (m/z: 154.02), naphtahlene (m/z: 127.01), $C_{11}H_{10}O_5N_2S$ (m/z: 281.98), $C_{11}H_9O_5NS$ (m/z: 265.97), and aniline (m/z: 93.02). Figure 21 shows the suggested photocatalytic degradation pathway scheme for Direct Orange 26 under visible light irradiation with $BiGdO_3$ as catalyst. It can be seen in Figure 21 that the chromophore cleavage, opening-ring and mineralization should be the main photocatalytic degradation pathway of Direct Orange 26 in this work. Direct Orange 26 was turned to smaller organic species, and then mineralized together with other organic groups to inorganic products such as CO_2, SO_4^{2-}, NH_4^+, N_2 and, ultimately, water.

3. Experimental Section

3.1. Preparation of BiGdO3

The $BiGdO_3$ sample was prepared by a solid-state reaction method, as was reported previously [112]. Bi_2O_3 and Gd_2O_3 with purity of 99.99% (Sinopharm Group Chemical Reagent Co., Ltd., Shanghai, China) were utilized as starting materials. Owing to the volatility of Bi_2O_3, we finally decided to add 115.6% quantities of Bi_2O_3 after 5 experiments. All powders were dried at 200 °C for 4 h before synthesis. In order to synthesize $BiGdO_3$, the precursors were stoichiometrically mixed, then pressed into small columns and put into an alumina crucible (Shenyang Crucible Co., Ltd., Shenyang, China). After the raw materials calcining at 750 °C for 10 h, we took the small columns out of the electric furnace, ground the mixed materials and then put into an electric furnace (KSL 1700X, Hefei Kejing Materials Technology Co., Ltd., Hefei, China). After the ground materials were calcined at 850 °C for 10 h, we took the small columns out of the electric furnace, ground the mixed materials and then put them into the electric furnace again. The mixed materials were calcined at 1050 °C for 12 h with an intermediate regrinding process in an electric furnace. Finally, pure $BiGdO_3$ catalyst, which presented the color of light orange, was obtained after total grinding. The cost of 100 g Gd_2O_3 or Bi_2O_3 was 63.2 and 64.5 dollars, respectively, while the synthesis of 100 g pure $BiGdO_3$ catalyst totally cost about 71 dollars.

3.2. Characterization of BiGdO3

The crystal structure of $BiGdO_3$ was analyzed by the powder X-ray diffraction method (XRD, XRD 6000, Shimadzu Corporation, Kyoto, Japan) with Cu$K\alpha$ radiation (λ = 1.54056 angstrom). The data were collected at 295 K with a step-scan procedure within the range of 2θ = 10°–100°. The step interval was 0.02° and the time per step was 1.2 s. The Bi^{3+} content, Gd^{3+} content and O^{2-} content of $BiGdO_3$ were determined by X-ray photoelectron spectroscopy (XPS, PHI 5000 Versa Probe, ULVAC-PHI Corporation, Kanagawa, Japan). The chemical composition within the depth profile of $BiGdO_3$ was detected by the argon ion denudation method when X-ray photoelectron spectroscopy was utilized. The particle morphology was detected by transmission electron microscope (TEM, JEM-200CX, JEOL Corporation, Tokyo, Japan). The chemical composition of $BiGdO_3$ was examined by scanning electron microscope-X-ray energy dispersion spectrum (SEM-EDS, 1530 VP, LEO Corporation, Dresden, Germany). The surface area of $BiGdO_3$ particle was measured by the Brunauer-Emmett-Teller method (BET, ASAP 2020, Micromeritics Corporation, Atlanta, GA, USA) with N_2 adsorption at liquid nitrogen temperature. Totally, 0.6 g $BiGdO_3$ was used to measure the surface area of $BiGdO_3$ every time. UV-Vis diffuse reflectance spectroscopy measurement of $BiGdO_3$ was carried out using an UV-Vis spectrophotometer (DRS, UV-2550, Shimadzu Corporation).

3.3. Photocatalytic Experiments

The photocatalytic activity of $BiGdO_3$ sample was evaluated by the degradation of Direct Orange 26 (DO-26, $C_{33}H_{22}N_6Na_2O_9S_2$) or Direct Red 23 (DR-23, $C_{35}H_{27}N_7O_{10}S_2$) (AR, Jiangsu Suzhou

TLRLHX CO., Ltd., Suzhou, China) in aqueous solution under visible light irradiation ($\lambda > 420$ nm). The photocatalytic reaction system was composed of a 500 W Xe arc lamp (Jiangsu Nanjing XJJD Co., Ltd., Nanjing, China), a magnetic stirrer and a cut-off filter ($\lambda > 420$ nm, Jiangsu Nanjing XJJD Co., Ltd.). The Xe arc lamp was surrounded by an outer recycling water quartz jacket so that the reaction temperature was maintained at near 25 °C by cooling water in the jacket. The cooling water jacket was surrounded by twelve quartz tubes (50 mL in volume), in which suspensions of direct dyes and photocatalysts were contained. The solution was continuously stirred with a low rate for better light irradiation by the operation of the magnetic stirrer below during the reaction. Prior to light irradiation, the suspension was magnetically stirred in the darkness for 30 min to reach adsorption/desorption equilibrium between the dye and the surface of the catalyst. The reactor was put in the air-saturated conditions to ensure enough oxygen in the reaction solution. The suspension pH values were adjusted to the desired level by using dilute NaOH and HCl, and then the pH values were measured with pH meter (Jiangsu Nanjing ASTKJFZ Co., Ltd., Nanjing, China). During visible light irradiation, one of the quartz tubes was sampled at certain time interval and centrifuged to remove solid particles. The filtrate was analyzed according to the absorption which was measured by a UV-Vis spectrophotometer (UV-2450, Shimadzu Corporation) at a certain wavelength in the UV-Vis spectra of the dyes. Using this method, the conversion percentage of dyes could be obtained at different intervals. The degree of degradation efficiency (*DE*, %) as a function of time was given as follows:

$$DE/\% = (C_0 - C_t)/C_0 \times 100\% \tag{12}$$

where C_0 was the initial concentration of the dyes, and C_t was the instant concentration in the sample. The total organic carbon (TOC) concentration was determined with a TOC analyzer (TOC-5000, Shimadzu Corporation).

Intermediate products of Direct Orange 26 were also identified by liquid chromatograph—mass spectrometer (LC-MS, Thermo Quest LCQ Duo, Silicon Valley, CA, USA, HPLC column: β Basic-C18 (150 mm × 2.1 mm × 5 μm), Finnigan, Thermo, Silicon Valley, CA, USA). Here, 20 μL of post-photocatalysis solution was injected automatically into the LC-MS system. The eluent contained 60% methanol and 40% water, and the flow rate was 0.2 mL·min^{-1}. MS conditions included an electrospray ionization interface and a capillary temperature of 27 °C with a voltage of 19.00 V, a spray voltage of 5000 V and a constant sheath gas flow rate. The spectrum was acquired in the negative ion scan mode, sweeping the *m/z* range from 50 to 600.

4. Conclusions

This work indicated the structural properties, optical properties and photocatalytic activity of $BiGdO_3$, which was prepared by a solid state reaction method. Structural characterization of the $BiGdO_3$ sample demonstrated that $BiGdO_3$ crystallized with the fluorite-type structure, face-centered cubic crystal system and space group *Fm3m 225*. The lattice parameter α for $BiGdO_3$ was 5.465 angstrom. UV-Vis diffuse reflectance spectra of $BiGdO_3$ displayed that $BiGdO_3$ showed a strong optical absorption in the visible light region and the band gap of $BiGdO_3$ was estimated to be 2.25 eV. $BiGdO_3$ indicated efficient photocatalytic activity for degrading Direct Orange 26 or Direct Red 23 in aqueous solution under visible light irradiation. The photocatalytic degradation efficiency was 83.7% for Direct Orange 26 and 60.8% for Direct Red 23 using $BiGdO_3$ as photocatalyst after visible light irradiation of 360 min. The photocatalytic degradation of Direct Orange 26 or Direct Red 23 followed the first-order reaction kinetics, and the first-order rate constant was 0.0046 or 0.0023 min^{-1} with $BiGdO_3$ as catalyst. The degradation intermediates of Direct Orange 26 were observed and the possible photocatalytic degradation pathway of Direct Orange 26 under visible light irradiation was provided. The stability of both material and performance of $BiGdO_3$ was investigated by material characterization and repeated photocatalytic degradation tests. The results showed that $BiGdO_3$ possessed excellent stability and was considered to be an efficient catalyst. $BiGdO_3$/(visible light) photocatalysis system was confirmed to be suitable for textile industry wastewater treatment.

The new photocatalyst BiGdO$_3$ which was prepared in this present paper and some relevant technical means were beneficial to some engineers or scientists who were engaged in printing and dyeing industry for the purpose of further wastewater treatment. In order to remove organic pollutants from dyes in the actual printing and dyeing wastewater, more improved methods should be implemented as follows: First, a high temperature electric furnace with the maximum sintering temperature of 1400 °C should be purchased. Second, it is important that three-step sintering grinding method be used to synthetize purely single phase BiGdO$_3$. During the whole process of preparation of BiGdO$_3$, we should pay attention to the increase of heating speed, the control of the maximum sintering temperature and holding time, and the reduction of cooling rate for obtaining the photocatalyst BiGdO$_3$ that has perfect crystallinity. Third, for the sake of economizing cost and maximizing the output, we could effectively deal with the actual printing and dyeing wastewater using BiGdO$_3$ as a new photocatalyst under the solar light irradiation. Finally, if the concentration of the organic pollutants that exist within actual printing and dyeing wastewater is too high (exceeded 1 mmol/L), we could diluted the printing and dyeing wastewater with pure water to obtain a low concentration of the organic pollutants and then utilized the photocatalyst BiGdO$_3$ and the solar light as advanced wastewater treatment technique to degrade the organic pollutants from dyes that exist within the actual printing and dyeing wastewater. All in all, the new photocatalyst BiGdO$_3$ that was prepared in this present paper could be applied to the advanced wastewater treatment of low concentration of the organic pollutants that existed within the actual printing and dyeing wastewater.

Author Contributions: Jingfei Luan was involved with all aspects of the study including conception, design, data interpretation and writing the manuscript. Yue Shen, Lingyan Zhang and Ningbin Guo performed the experiments and analyzed data. Jingfei Luan and Yue Shen wrote the paper. All authors read and approved the manuscript.

Conflicts of Interest: The authors declare no conflict of interest.

References

1. Liu, J.; Liu, Y.; Liu, N.Y.; Liu, N.; Han, Y.; Zhang, X.; Huangf, H.; Lifshitz, Y.; Lee, S.-T.; Zhong, J.; et al. Metal-free efficient photocatalyst for stable visible water splitting via a two-electron pathway. *Science* **2015**, *347*, 970–974. [CrossRef] [PubMed]

2. Jaiswal, R.; Patel, N.; Dashora, A.; Fernandes, R.; Yadav, M.; Edla, R.; Varma, R.S.; Kothari, D.C.; Ahuja, B.L.; Miotello, A. Efficient Co-B-codoped TiO$_2$ photocatalyst for degradation of organic water pollutant under visible light. *Appl. Catal. B* **2016**, *183*, 242–253. [CrossRef]

3. Colmenares, J.C.; Kuna, E.; Jakubiak, S.; Michalski, J.; Kurzydlowski, K. Polypropylene nonwoven filter with nanosized ZnO rods: Promising hybrid photocatalyst forwater purification. *Appl. Catal. B* **2015**, *170*, 273–282. [CrossRef]

4. Kuwahara, Y.; Aoyama, J.; Miyakubo, K.; Eguchi, T.; Kamegawa, T.; Mori, K.; Yamashita, H. TiO$_2$ photocatalyst for degradation of organic compounds in water and air supported on highly hydrophobic FAU zeolite: Structural, sorptive, and photocatalytic studies. *J. Catal.* **2012**, *285*, 223–234. [CrossRef]

5. Venieri, D.; Fraggedaki, A.; Kostadima, M.; Chatzisymeon, E.; Binas, V.; Zachopoulosb, A.; Kiriakidisb, G.; Mantzavinosd, D. Solar light and metal-doped TiO$_2$ to eliminate water-transmitted bacterial pathogens: Photocatalyst characterization and disinfection performance. *Appl. Catal. B* **2014**, *154*, 93–101. [CrossRef]

6. Mueses, M.A.; Machuca-Martinez, F.; Puma, G. Effective quantum yield and reaction rate model for evaluation of photocatalytic degradation of water contaminants in heterogeneous pilot-scale solar photoreactors. *Chem. Eng. J.* **2013**, *215*, 937–947. [CrossRef]

7. Luan, J.F.; Chen, M.J.; Hu, W.H. Synthesis, characterization and photocatalytic activity of new photocatalyst ZnBiSbO$_4$ under visible light irradiation. *Int. J. Mol. Sci.* **2014**, *15*, 9459–9480. [CrossRef] [PubMed]

8. Srinivasu, K.; Modak, B.; Ghosh, S.K. Porous graphitic carbon nitride: A possible metal-free photocatalyst for water splitting. *J. Phys. Chem. C* **2014**, *118*, 26479–26484. [CrossRef]

9.　Jin, S.Q.; Wang, X.; Wang, X.L.; Ju, M.G.; Shen, S.; Liang, W.Z.; Zhao, Y.; Feng, Z.C.; Playford, H.Y.; Walton, R.I. Effect of phase junction structure on the photocatalytic performance in overall water splitting: Ga_2O_3 photocatalyst as an example. *J. Phys. Chem. C* **2015**, *119*, 18221–18228. [CrossRef]

10.　Hirayama, J.; Abe, R.; Kamiya, Y. Combinational effect of $Pt/SrTiO_3$: Rh photocatalyst and $SnPd/Al_2O_3$ non-photocatalyst for photocatalytic reduction of nitrate to nitrogen in water under visible light irradiation. *Appl. Catal. B* **2014**, *144*, 721–729. [CrossRef]

11.　Daneshvar, N.; Behnajady, M.A.; Asghar, Y.Z. Photooxidative degradation of 4-nitrophenol (4-NP) in UV/H_2O_2 process: Influence of operational parameters and reaction mechanism. *J. Hazard. Mater.* **2007**, *139*, 275–279. [CrossRef]

12.　Lee, K.M.; Lai, C.W.; Ngai, K.S.; Juan, J.C. Recent developments of zinc oxide based photocatalyst in water treatment technology: A review. *Water Res.* **2016**, *88*, 428–448. [CrossRef] [PubMed]

13.　Wakimoto, R.; Kitamura, T.; Ito, F.; Usami, H.; Moriwaki, H. Decomposition of methyl orange using C-60 fullerene adsorbed on silica gel as a photocatalystvia visible-light induced electron transfer. *Appl. Catal. B* **2015**, *166*, 544–550. [CrossRef]

14.　Parida, K.M.; Sahu, N.; Biswal, N.R.; Naik, B.; Pradhan, A.C. Preparation, characterization, and photocatalytic activity of sulfate-modified titania for degradation of methyl orange under visible light. *J. Colloid Interface Sci.* **2008**, *318*, 231–237. [CrossRef] [PubMed]

15.　Sun, H.Q.; Liu, S.Z.; Liu, S.M.; Wang, S.B. A comparative study of reduced graphene oxide modified TiO_2, ZnO and Ta_2O_5 in visible light photocatalytic/photochemical oxidation of methylene blue. *Appl. Catal. B* **2014**, *146*, 162–168. [CrossRef]

16.　Yoshinaga, M.; Yamamoto, K.; Sato, N.; Aoki, K.; Morikawa, T.; Muramatsu, A. Remarkably enhanced photocatalytic activity by nickel nanoparticle deposition on sulfur-doped titanium dioxide thin film. *Appl. Catal. B* **2009**, *87*, 239–244. [CrossRef]

17.　Sathyaseelan, B.; Manikandan, E.; Lakshmanan, V.; Baskaran, I.; Sivakumar, K.; Ladchumananandasivam, R.; Kennedy, J.; Maaza, M. Structural, optical and morphological properties of post-growth calcined TiO_2 nanopowder for opto-electronic device application: Ex-situ studies. *J. Alloy. Compd.* **2016**, *671*, 486–492. [CrossRef]

18.　Erjavec, B.; Hudoklin, P.; Perc, K.; Tisler, T.; Dolenc, M.S.; Pintar, A. Glass fiber-supported TiO_2 photocatalyst: Efficient mineralization and removal of toxicity/estrogenicity of bisphenol A and its analogs. *Appl. Catal. B* **2016**, *183*, 149–158. [CrossRef]

19.　Hajkova, P.; Matousek, J.; Antos, P. Aging of the photocatalytic TiO_2 thin films modified by Ag and Pt. *Appl. Catal. B* **2014**, *160*, 51–56. [CrossRef]

20.　Yaghoubi, H.; Li, Z.; Chen, Y.; Ngo, H.T.; Bhethanabotla, V.R.; Joseph, B.; Ma, S.Q.; Schlaf, R.; Takshi, A. Toward a visible light-driven photocatalyst: The effect of midgap-states-induced energy gap of undoped TiO_2 nanoparticles. *ACS Catal.* **2015**, *5*, 327–335. [CrossRef]

21.　Yao, B.H.; Peng, C.; Zhang, W.; Zhang, Q.K.; Niu, J.F.; Zhao, J.E. A novel Fe(III) porphyrin-conjugated TiO_2 visible-light photocatalyst. *Appl. Catal. B* **2015**, *174*, 77–84. [CrossRef]

22.　Wang, W.J.; Li, Y.C.; Kang, Z.W.; Wang, F.; Yu, J.C. A NIR-driven photocatalyst based on α-$NaYF_4$: Yb,Tm@TiO_2 core-shell structure supported on reduced graphene oxide. *Appl. Catal. B* **2016**, *182*, 184–192. [CrossRef]

23.　Cong, Y.; Zhang, J.; Chen, F.; Anpo, M. Synthesis and characterization of nitrogen-doped TiO_2 nanophotocatalyst with high visible light activity. *J. Phys. Chem. C* **2007**, *111*, 6976–6982. [CrossRef]

24.　Ren, F.Z.; Li, H.Y.; Wang, Y.X.; Yang, J.J. Enhanced photocatalytic oxidation of propylene over V-doped TiO_2 photocatalyst: Reaction mechanism between V^{5+} and single-electron-trapped oxygen vacancy. *Appl. Catal. B* **2015**, *176*, 160–172. [CrossRef]

25.　Zhou, W.Y.; Cao, Q.Y.; Tang, S.Q.; Liu, Y.J. Doping mechanism and visible-light photocatalytic activity of S-doped TiO_2 nano powders. *J. Inorg. Mater.* **2006**, *21*, 776–782.

26.　Zhang, P.; Fujitsuka, M.; Majima, T. TiO_2 mesocrystal with nitrogen and fluorine codoping during topochemical transformation: efficient visible light induced photocatalyst with the codopants. *Appl. Catal. B* **2015**, *185*, 181–188. [CrossRef]

27.　Wang, Z.P.; Cai, W.M.; Hong, X.T.; Zhao, X.L.; Xu, F.; Cai, C.G. Photocatalytic degradation of phenol in aqueous nitrogen-doped TiO_2 suspensions with various light sources. *Appl. Catal. B* **2005**, *57*, 223–231. [CrossRef]

28.　Liu, L.Q.; Dao, T.D.; Kodiyath, R.; Kang, Q.; Abe, H.; Nagao, T.; Ye, J.H. Plasmonic janus-composite photocatalyst comprising Au and C-TiO_2 for enhanced aerobic oxidation over a broad visible-light range. *Adv. Funct. Mater.* **2014**, *24*, 7754–7762. [CrossRef]

29. Jaiswal, R.; Bharambe, J.; Patel, N.; Dashora, A.; Kothari, D.C.; Miotello, A. Copper and Nitrogen co-doped TiO_2 photocatalyst with enhanced optical absorption and catalytic activity. *Appl. Catal. B* **2015**, *168*, 333–341. [CrossRef]

30. Qi, D.Y.; Xing, M.Y.; Zhang, J.L. Hydrophobic carbon-doped TiO_2/MCF-F composite as a high performance photocatalyst. *J. Phys. Chem. C* **2014**, *118*, 7329–7336. [CrossRef]

31. Zhang, L.J.; Zhou, J.; Li, J.; Liu, G.; Lin, X.; Mao, B.H.; Liu, R.D.; Zhang, S.; Wang, J.Q. Surface structural reconstruction for optical response in iodine-modified TiO_2 photocatalyst system. *J. Phys. Chem. C* **2014**, *118*, 13726–13732. [CrossRef]

32. Ghaffar, I.; Warsi, M.F.; Shahid, M.; Shakir, I. Unprecedented photocatalytic activity of carbon coated/MoO_3 core-shell nanoheterostructurs under visible light irradiation. *Physica E* **2016**, *79*, 1–7. [CrossRef]

33. Nazim, S.; Kousar, T.; Shahid, M.; Khan, M.A.; Nasar, G.; Sher, M.; Warsi, M.F. New graphene-CoxZn$_1$-xFe$_2$O$_4$ nano-heterostructures: Magnetically separable visible lightphotocatalytic materials. *Ceram. Int.* **2016**, *42*, 7647–7654. [CrossRef]

34. Zhang, Y.F.; Qiu, L.G.; Yuan, Y.P.; Zhu, Y.J.; Jiang, X.; Xiao, J.D. Magnetic Fe_3O_4@C/Cu and Fe_3O_4@CuO core-shell composites constructed from MOF-based materials and their photocatalytic properties under visible light. *Appl. Catal. B* **2014**, *144*, 863–869. [CrossRef]

35. Yu, C.L.; Yang, K.; Shu, Q.; Yu, J.C.; Cao, F.F.; Li, X. Preparation of WO_3/ZnO composite photocatalyst and its photocatalytic performance. *Chin. J. Catal.* **2011**, *32*, 555–565. [CrossRef]

36. Tanaka, A.; Hashimoto, K.; Kominami, H. Visible-light-induced hydrogen and oxygen formation over Pt/Au/WO_3 photocatalyst utilizing two types of photoabsorption due to surface plasmon resonance and band-gap excitation. *J. Am. Chem. Soc.* **2014**, *136*, 586–589. [CrossRef] [PubMed]

37. Xia, S.J.; Zhang, L.Y.; Zhou, X.B.; Shao, M.M.; Pan, G.X.; Ni, Z.M. Fabrication of highly dispersed Ti/ZnO-Cr_2O_3 composite as highly efficient photocatalyst for naphthalene degradation. *Appl. Catal. B* **2015**, *176*, 266–277. [CrossRef]

38. Zhang, A.Y.; Wang, W.K.; Pei, D.N.; Yu, H.Q. Degradation of refractory pollutants under solar light irradiation by a robust and self-protected ZnO/CdS/TiO_2 hybrid photocatalyst. *Water Res.* **2016**, *92*, 78–86. [CrossRef] [PubMed]

39. Savio, A.K.P.D.; Fletcher, J.; Smith, K.; Iyer, R.; Bao, J.M.; Hernandez, F.C.R. Environmentally effective photocatalyst CoO-TiO_2 synthesized by thermal precipitation of Co in amorphous TiO. *Appl. Catal. B* **2016**, *182*, 449–455. [CrossRef]

40. Wang, Y.F.; Jiao, A.F.; Ding, G.Y.; Fan, C.M. Preparation and photocatalytic properties of CuO/SnO_2/TiO_2 composite photocatalysts. *J. Synth. Cryst.* **2010**, *39*, 401–406.

41. Obregon, S.; Zhang, Y.F.; Colon, G. Cascade charge separation mechanism by ternary heterostructured $BiPO_4$/TiO_2/g-C_3N_4 photocatalyst. *Appl. Catal. B* **2016**, *184*, 96–103. [CrossRef]

42. Wei, Q.L.; Zhao, X.L.; Yao, P.P.; Mu, J. Preparation and visible light photocatalytic activity of $AgInS_2$ nanoparticles. *Chin. J. Inorg. Chem.* **2011**, *27*, 692–696.

43. Kameyama, T.; Takahashi, T.; Machida, T.; Kamiya, Y.; Yamamoto, T.; Kuwabata, S.; Torimoto, T. Controlling the electronic energy structure of ZnS-$AgInS_2$ solid solution nanocrystals for photoluminescence and photocatalytic hydrogen evolution. *J. Phys. Chem. C* **2015**, *119*, 24740–24749. [CrossRef]

44. Liu, W.; Ji, M.S.; Chen, S.F. Preparation, characterization and activity evaluation of $Ag_2Mo_4O_{13}$ photocatalyst. *J. Hazard. Mater.* **2011**, *186*, 2001–2008. [CrossRef] [PubMed]

45. Zhang, G.K.; Zou, X.; Gong, J.; He, F.S.; Zhang, H.; Zhang, Q.; Liu, Y.; Yang, X.; Hu, B. Preparation and photocatalytic property of potassium niobate $K_6Nb_{10.8}O_{30}$. *J. Alloy. Compd.* **2006**, *425*, 76–80. [CrossRef]

46. Li, K.W.; Wang, H.; Yan, H. Hydrothermal preparation and photocatalytic properties of $Y_2Sn_2O_7$ nanocrystals. *J. Mol. Catal. A: Chem.* **2006**, *249*, 65–70. [CrossRef]

47. Zhang, L.W.; Fu, H.B.; Zhang, C.; Zhu, Y.F. Effects of Ta^{5+} substitution on the structure and photocatalytic behavior of the $Ca_2Nb_2O_7$ photocatalyst. *J. Phys. Chem. C* **2008**, *112*, 3126–3133. [CrossRef]

48. Luan, J.F.; Zou, Z.G.; Lu, M.H.; Zheng, S.R.; Chen, Y.F. Growth, structural and photophysical properties of Bi_2GaTaO_7. *J. Cryst. Growth* **2004**, *273*, 241–247. [CrossRef]

49. Mishra, Y.K.; Modi, G.; Cretu, V.; Postica, V.; Lupan, O.; Reimer, T.; Paulowicz, I.; Hrkac, V.; Benecke, W.; Kienle, L. Direct growth of freestanding ZnO Tetrapod networks for multifunctional applications in photocatalysis, UV photodetection, and gas sensing. *ACS Appl. Mater. Int.* **2015**, *7*, 14303–14316. [CrossRef] [PubMed]

50. Reimer, T.; Paulowicz, I.; Roder, R.; Kaps, S.; Lupan, O.; Chemnitz, S.; Benecke, W.; Ronning, C.; Adelung, R.; Mishra, Y.K. Single step integration of ZnO nano- and microneedles in Si trenches by novel flame transport approach: Whispering gallery modes and photocatalytic properties. *ACS Appl. Mater. Int.* **2014**, *6*, 7806–7815. [CrossRef] [PubMed]

51. Addorisio, V.; Esposito, S.; Sannino, F. Sorption capacity of mesoporous metal oxides for the removal of MCPA from polluted waters. *J. Agric. Food Chem.* **2010**, *58*, 5011–5016. [CrossRef] [PubMed]

52. Moniz, S.J.A.; Blackman, C.S.; Carmalt, C.J.; Hyett, G. MOCVD of crystalline Bi_2O_3 thin films using a single-source bismuth alkoxide precursor and their use in photodegradation of water. *J. Mater. Chem.* **2010**, *20*, 7881–7886. [CrossRef]

53. Wang, Y.J.; He, Y.M.; Li, T.T.; Cai, J.; Luo, M.F.; Zhao, L.H. Photocatalytic degradation of methylene blue on $CaBi_6O_{10}/Bi_2O_3$ composites under visible light. *Chem. Eng. J.* **2012**, *189*, 473–481. [CrossRef]

54. Muruganandham, M.; Amutha, R.; Lee, G.J.; Hsieh, S.H.; Wu, J.J.; Sillanpää, M. Facile fabrication of tunable Bi_2O_3 self-assembly and its visible light photocatalytic activity. *J. Phys. Chem. C* **2012**, *116*, 12906–12915. [CrossRef]

55. Pei, C.C.; Leung, W.W.F. Photocatalytic oxidation of nitrogen monoxide and *O*-xylene by $TiO_2/ZnO/Bi_2O_3$ nanofibers: Optimization, kinetic modeling and mechanisms. *Appl. Catal. B* **2015**, *174*, 515–525. [CrossRef]

56. Hameed, A.; Aslam, M.; Ismail, I.M.I.; Salah, N.; Fornasiero, P. Sunlight induced formation of surface Bi_2O_4-x-Bi_2O_3 nanocomposite during the photocatalytic mineralization of 2-chloro and 2-nitrophenol. *Appl. Catal. B* **2015**, *163*, 444–451. [CrossRef]

57. Huang, Y.C.; Fan, W.J.; Long, B.; Li, H.B.; Zhao, F.Y.; Liu, Z.L.; Tong, Y.X.; Ji, H.B. Visible light $Bi_2S_3/Bi_2O_3/Bi_2O_2CO_3$ photocatalyst for effective degradation of organic pollutions. *Appl. Catal. B* **2016**, *185*, 68–76. [CrossRef]

58. Zhu, G.Q.; Que, W.X.; Zhang, J. Synthesis and photocatalytic performance of Ag-loaded β-Bi_2O_3 microspheres under visible light irradiation. *J. Alloy. Compd.* **2011**, *509*, 9479–9486. [CrossRef]

59. Ding, Y.B.; Yang, F.; Zhu, L.H.; Wang, N.; Tang, H.Q. Bi^{3+} self doped $NaBiO_3$ nanosheets: Facile controlled synthesis and enhanced visible light photocatalytic activity. *Appl. Catal. B* **2015**, *164*, 151–158. [CrossRef]

60. Jiang, H.Y.; Liu, G.; Li, M.; Liu, J.J.; Sun, W.B.; Ye, J.H.; Lin, J. Efficient organic degradation under visible light by α-Bi_2O_3 with a CuO_x-assistant electron transfer process. *Appl. Catal. B* **2015**, *163*, 267–276. [CrossRef]

61. Zhang, X.; Ai, Z.H.; Jia, F.L.; Zhang, L.Z.; Fan, X.X.; Zou, Z.G. Selective synthesis and visible-light photocatalytic activities of $BiVO_4$ with different crystalline phases. *Mater. Chem. Phys.* **2007**, *103*, 162–167.

62. Ji, K.M.; Dai, H.X.; Deng, J.G.; Zang, H.J.; Arandiyan, H.; Xie, S.H.; Yang, H.G. 3DOM $BiVO_4$ supported silver bromide and noble metals: high-performance photocatalysts for the visible-light-driven degradation of 4-chlorophenol. *Appl. Catal. B* **2015**, *168*, 274–282. [CrossRef]

63. Saison, T.; Chemin, N.; Chanéac, C.; Durupthy, O.; Ruaux, V.; Mariey, L.; Maugé, F.; Beaunier, P.; Jolivet, J.P. Bi_2O_3, $BiVO_4$, and Bi_2WO_6: Impact of surface properties on photocatalytic activity under visible light. *J. Phys. Chem. C* **2011**, *115*, 5657–5666. [CrossRef]

64. Li, C.M.; Chen, G.; Sun, J.X.; Dong, H.J.; Wang, Y.; Lv, C. Construction of Bi_2WO_6 homojunction via QDs self-decoration and its improved separation efficiency of charge carriers and photocatalytic ability. *Appl. Catal. B* **2014**, *160*, 383–389. [CrossRef]

65. Murugesan, S.; Subramanian, V. Robust synthesis of bismuth titanate pyrochlore nanorods and their photocatalytic applications. *Chem. Commun.* **2009**, *34*, 5109–5111. [CrossRef] [PubMed]

66. Allured, B.; DelaCruz, S.; Darling, T.; Huda, M.N.; Subramanian, V. Enhancing the visible light absorbance of $Bi_2Ti_2O_7$ through Fe-substitution and its effects on photocatalytic hydrogen evolution. *Appl. Catal. B* **2014**, *144*, 261–268. [CrossRef]

67. Zhou, J.K.; Zou, Z.G.; Ray, A.K.; Zhao, X.S. Preparation and characterization of polycrystalline bismuth titanate $Bi_{12}TiO_{20}$ and its photocatalytic properties under visible light irradiation. *Ind. Eng. Chem. Res.* **2007**, *46*, 745–749. [CrossRef]

68. Su, W.N.; Ayele, D.W.; Ochie, V.; Pan, C.J.; Hwang, B.J. The development of highly crystalline single-phase $Bi_{20}TiO_{32}$ nanoparticles for light driven oxygen evolution. *Appl. Catal. B* **2014**, *150*, 363–369. [CrossRef]

69. Luan, J.F.; Zou, Z.G.; Lu, M.H.; Luan, G.Y.; Chen, Y.F. Structural and photocatalytic properties of the new solid photocatalyst In_2BiTaO_7. *Res. Chem. Intermed.* **2006**, *32*, 31–42. [CrossRef]

70. Wang, Y.; Wang, Y.; Meng, Y.L.; Ding, H.M.; Shan, Y.K. A highly efficient visible-light-activated photocatalyst based on bismuth- and sulfur-codoped TiO_2. *J. Phys. Chem. C* **2008**, *112*, 6620–6626. [CrossRef]

71. Long, M.C.; Hu, P.D.; Wu, H.D.; Cai, J.; Tan, B.H.; Zhou, B.X. Efficient visible light photocatalytic heterostructure of nonstoichiometric bismuth oxyiodide and iodine intercalated $Bi_2O_2CO_3$. *Appl. Catal. B* **2016**, *184*, 20–27. [CrossRef]

72. Guo, R.Q.; Fang, L.; Dong, W.; Zheng, F.G.; Shen, M.R. Enhanced photocatalytic activity and ferromagnetism in Gd doped $BiFeO_3$ nanoparticles. *J. Phys. Chem. C* **2010**, *114*, 21390–21396. [CrossRef]

73. Luo, X.C.; Zhu, G.Q.; Peng, J.H.; Wei, X.M.; Hojamberdiev, M.; Jin, L.; Liu, P. Enhanced photocatalytic activity of Gd-doped porous β-Bi_2O_3 photocatalysts under visible light irradiation. *Appl. Surf. Sci.* **2015**, *351*, 260–269. [CrossRef]

74. Xu, J.J.; Ao, Y.H.; Fu, D.G.; Yuan, C.W. Synthesis of Gd-doped TiO_2 nanoparticles under mild condition and their photocatalytic activity. *Colloid. Surf. A* **2009**, *334*, 107–111. [CrossRef]

75. Zhang, N.; Chen, D.; Niu, F.; Wang, S.; Qin, L.S.; Huang, Y.X. Enhanced visible light photocatalytic activity of Gd-doped $BiFeO_3$ nanoparticles and mechanism insight. *Sci. Rep-UK* **2016**. [CrossRef] [PubMed]

76. Shimodaira, Y.; Kato, H.; Kobayashi, H.; Kudo, A. Photophysical properties and photocatalytic activities of bismuth molybdates under visible light irradiation. *J. Phys. Chem. B* **2006**, *110*, 17790–17797. [CrossRef] [PubMed]

77. He, G.P.; Xing, C.L.; Xiao, X.; Hu, R.P.; Zuo, X.X.; Nan, J.M. Facile synthesis of flower-like $Bi_{12}O_{17}Cl_2 / \beta$-$Bi_2O_3$ composites with enhanced visible light photocatalytic performance for the degradation of 4-tert-butylphenol. *Appl. Catal. B* **2015**, *170*, 1–9. [CrossRef]

78. Izumi, F. A software package for the rietveld analysis of X-ray and neutron diffraction patterns. *J. Crystallogr. Assoc. Jpn.* **1985**, *27*, 23–26. [CrossRef]

79. Bid, S.; Pradhan, S.K. Characterization of crystalline structure of ball-milled nano-Ni-Zn-ferrite by Rietveld method. *Mater. Chem. Phys.* **2004**, *84*, 291–301. [CrossRef]

80. Yang, X.; Yang, L.Y.; Lin, S.Y.; Zhou, R.X. New insight into the doping effect of Pr_2O_3 on the structure-activity relationship of Pd/CeO_2-ZrO_2 catalysts by raman and XRD rietveld analysis. *J. Phys. Chem. C* **2015**, *119*, 6065–6074. [CrossRef]

81. Liao, Y.H.B.; Wang, J.X.; Lin, J.S.; Chung, W.H.; Lin, W.Y.; Chen, C.C. Synthesis, photocatalytic activities and degradation mechanism of Bi_2WO_6 toward crystal violet dye. *Catal. Today* **2011**, *174*, 148–159. [CrossRef]

82. Muktha, B.; Priya, M.H.; Madras, G.; Row, T.N.G. Synthesis, structure, and photocatalysis in a new structural variant of the Aurivillius phase: $LiBi_4M_3O_{14}$ (M = Nb, Ta). *J. Phys. Chem. B* **2005**, *109*, 11442–11449. [CrossRef] [PubMed]

83. Oshikiri, M.; Boero, M.; Ye, J.H.; Zou, Z.G.; Kido, G. Electronic structures of promising photocatalysts $InMO_4$ (M = V, Nb, Ta) and $BiVO_4$ for water decomposition in the visible wavelength region. *J. Chem. Phys.* **2002**, *117*, 7313–7318.

84. Zheng, S.K.; Wu, Y.; Zhang, M.J.; Li, W.M.; Yan, X.B. Electronic structure of Gd/N co-doped anatase TiO_2 by first-principles calculations. *Ceram. Int.* **2015**, *41*, 13861–13866. [CrossRef]

85. Luan, J.F.; Li, M.; Ma, K.; Li, Y.M.; Zou, Z.G. Photocatalytic activity of novel Y_2InSbO_7 and Y_2GdSbO_7 nanocatalysts for degradation of environmental pollutant rhodamine B under visible light irradiation. *Chem. Eng. J.* **2011**, *167*, 162–171. [CrossRef]

86. Luan, J.F.; Zou, Z.; Lu, M.; Chen, Y. Structural, optical and photocatalytic properties of new solid photocatalysts, $Bi_xIn_{1-x}TaO_4$ (0 < x < 1). *Mater. Chem. Phys.* **2006**, *98*, 434–441.

87. Tauc, J.; Grigorovici, R.; Vancu, A. Optical properties and electronic structure of amorphous germanium. *Phys. Status Solidi* **1966**, *15*, 627–637. [CrossRef]

88. Butler, M.A. Photoelectrolysis and physical-properties of semiconducting electrode WO_3. *J. Appl. Phys.* **1977**, *48*, 1914–1920. [CrossRef]

89. Calza, P.; Rigo, L.; Sangermano, M. Investigations of photocatalytic activities of photosensitive semiconductors dispersed into epoxy matrix. *Appl. Catal. B* **2011**, *106*, 657–663. [CrossRef]

90. Ao, Y.H.; Wang, K.D.; Wang, P.F.; Wang, C.; Hou, J. Synthesis of novel 2D-2D p-n heterojunction $BiOBr/La_2Ti_2O_7$ composite photocatalyst with enhanced photocatalytic performance under both UV and visible light irradiation. *Appl. Catal. B* **2016**, *194*, 157–168. [CrossRef]

91. Mangrulkar, P.A.; Kamble, S.P.; Joshi, M.M.; Meshram, J.S.; Labhsetwar, N.K.; Rayalu, S.S. Photocatalytic degradation of phenolics by N-doped mesoporous titania under solar radiation. *Int. J. Photoenergy* **2012**, *78*, 62–71. [CrossRef]

92. Vaiano, V.; Iervolino, G.; Sannino, D.; Murcia, J.J.; Hidalgo, M.C.; Ciambelli, P.; Navio, J.A. Photocatalytic removal of patent blue V dye on Au-TiO$_2$ and Pt-TiO$_2$ catalysts. *Appl. Catal. B* **2016**, *188*, 134–146. [CrossRef]

93. Jantawasu, P.; Sreethawong, T.; Chavadej, S. Photocatalytic activity of nanocrystalline mesoporous-assembled TiO$_2$ photocatalyst for degradation of methyl orange monoazo dye in aqueous wastewater. *Chem. Eng. J.* **2009**, *155*, 223–233. [CrossRef]

94. Konstantinou, I.K.; Albanis, T.A. TiO$_2$-assisted photocatalytic degradation of azo dyes in aqueous solution: Kinetic and mechanistic investigations-a review. *Appl. Catal. B* **2004**, *49*, 1–14. [CrossRef]

95. Guo, H.X.; Lin, K.L.; Zheng, Z.S.; Xiao, F.B.; Lia, S.X. Sulfanilic acid-modified P25 TiO$_2$ nanoparticles with improved photocatalytic degradation on Congo red under visible light. *Dyes Pigments* **2012**, *92*, 1278–1284. [CrossRef]

96. Liu, X.Y.; Xu, D.; Zhang, D.F.; Zhang, G.Z.; Zhang, L. Superior performance of 3 D Co-Ni bimetallic oxides for catalytic degradation of organic dye: investigation on the effect of catalyst morphology and catalytic mechanism. *Appl. Catal. B* **2016**, *186*, 193–203. [CrossRef]

97. Yuan, R.X.; Ramjaun, S.N.; Wang, Z.H.; Liu, J.S. Photocatalytic degradation and chlorination of azo dye in saline wastewater: Kinetics and AOX formation. *Chem. Eng. J.* **2012**, *192*, 171–178. [CrossRef]

98. Fujishima, A.; Zhang, X.T.; Tryk, D.A. TiO$_2$ photocatalysis and related surface phenomena. *Surf. Sci. Rep.* **2008**, *63*, 515–582. [CrossRef]

99. Ochiai, T.; Fujishima, A. Photoelectrochemical properties of TiO$_2$ photocatalyst and its applications for environmental purification. *J. Photochem. Photobiol. C* **2012**, *13*, 247–262. [CrossRef]

100. Habibi, M.H.; Hassanzadeh, A.; Mahdavi, S. The effect of operational parameters on the photocatalytic degradation of three textile azo dyes in aqueous TiO$_2$ suspensions. *J. Photochem. Photobiol. A* **2005**, *172*, 89–96. [CrossRef]

101. Eskandarian, M.R.; Choi, H.; Fazli, M.; Rasoulifard, M.H. Effect of UV-LED wavelengths on direct photolytic and TiO$_2$ photocatalytic degradation of emerging contaminants in water. *Chem. Eng. J.* **2016**, *300*, 414–422. [CrossRef]

102. Dotson, A.D.; Keen, V.S.; Metz, D.; Linden, K.G. UV/H$_2$O$_2$ treatment of drinking water increases post-chlorination DBP formation. *Water Res.* **2010**, *44*, 3703–3713. [CrossRef] [PubMed]

103. Ahmed, S.; Rasul, M.G.; Martens, W.N.; Brown, R.; Hashib, M.A. Advances in heterogeneous photocatalytic degradation of phenols and dyes in wastewater: A review. *Water Air Soil Pull.* **2011**, *215*, 3–29. [CrossRef]

104. Rioja, N.; Zorita, S.; Penas, F.J. Effect of water matrix on photocatalytic degradation and general kinetic modeling. *Appl. Catal. B* **2016**, *180*, 330–335. [CrossRef]

105. Hu, C.; Yu, J.C.; Hao, Z.; Wong, P.K. Effects of acidity and inorganic ions on the photocatalytic degradation of different azo dyes. *Appl. Catal. B* **2003**, *46*, 35–47. [CrossRef]

106. Deng, N.S.; Fang, T.; Tian, S.Z. Photodegradation of dyes in aqueous solutions containing Fe(III)-hydroxy complex: Photodegradation kinetics. *Chemosphere* **1996**, *33*, 547–557.

107. Chong, M.N.; Jin, B.; Laera, G.; Saint, C.P. Evaluating the photodegradation of Carbamazepine in a sequential batch photoreactor system: Impacts of effluent organic matter and inorganic ions. *Chem. Eng. J.* **2011**, *174*, 595–602. [CrossRef]

108. Gao, H.L.; Yan, S.C.; Wang, J.J.; Zou, Z.G. Inorganic ions promoted photocatalysis based on polymer photocatalyst. *Appl. Catal. B* **2014**, *158*, 321–328. [CrossRef]

109. Neppolian, B.; Choi, H.C.; Sakthivel, S.; Arabindoo, B.; Murugesan, V. Solar light induced and TiO$_2$ assisted degradation of textile dye reactive blue. *Chemosphere* **2002**, *46*, 1173–1181. [CrossRef]

110. Zhang, X.W.; Wang, Y.Z.; Li, G.T. Effect of operating parameters on microwave assisted photocatalytic degradation of azo dye X-3B with grain TiO$_2$ catalyst. *J. Mol. Catal. A-Chem.* **2005**, *237*, 199–205. [CrossRef]

111. Santiago, D.E.; Arana, J.; Gonzalez-Diaz, O.; Aleman-Dominguez, M.E.; Acosta-Dacal, A.C.; Fernandez-Rodriguez, C.; Perez-Pena, J.; Doña-Rodríguez, J.M. Effect of inorganic ions on the photocatalytic treatment of agro-industrial wastewaters containing imazalil. *Appl. Catal. B* **2014**, *156*, 284–292. [CrossRef]

112. Luan, J.F.; Zhang, L.Y.; Ma, K.; Li, Y.M.; Zou, Z.G. Preparation and property characterization of new Y$_2$FeSbO$_7$ and In$_2$FeSbO$_7$ photocatalysts. *Solid State Sci.* **2011**, *13*, 185–194. [CrossRef]